Materials Today Advances 28 (2025) 100656

Contents lists available at ScienceDirect

Materials Today Advances

journal homepage: www.sciencedirect.com/journal/materials-today-advances/

Force transmission and dissipation in dynamic compression of architected metamaterials

T. Gärtner [a,c,*], S.J. van den Boom [c,b], J. Weerheijm [a], L.J. Sluys [a]

[a] Faculty of Civil Engineering and Geosciences, Delft University of Technology, Stevingweg 1, 2628 CN Delft, The Netherlands
[b] Faculty of Mechanical Engineering, Delft University of Technology, Mekelweg 2, 2628 CD Delft, The Netherlands
[c] Netherlands Institute for Applied Scientific Research (TNO), Postbus 480, 2501 CL Den Haag, The Netherlands

ARTICLE INFO

Keywords:
Architected materials
Impact mitigation
Strain-rate effects
Elasto-plastic beams
Dynamic compression

ABSTRACT

Materials engineered with an internal architecture in order to achieve unusual properties, so-called mechanical metamaterials, are a promising candidate in the ongoing quest for lightweight impact mitigation. During impact events, these materials are subject to high strain rates, and the forces occurring due to the deceleration of the impactor are transmitted in a non-uniform way. The prevailing research in the field of impact mitigation focuses largely on the global effects of architected materials, with less attention being paid to the internal mechanisms of these structured materials. While there have been recent studies on the distribution of forces throughout an impact event, less research is devoted to the transmission of forces and the distribution of energy dissipation. The objective of this study is to examine the transition from static deformation patterns to dynamic phenomena for different types and sizes of microstructure, and to understand both the force transmission through the patch and the energetic distributions in different strain rate regimes. To enable this investigation discretized — geometrically as well as materially — nonlinear Timoshenko-Ehrenfest beams are used in implicit and explicit finite element schemes. The transmitted force levels and energy dissipation are investigated for two auxetic architectures (one for each mechanism resulting in a negative Poisson's ratio) and one non-auxetic architecture. The dynamic force levels transmitted to the back face exhibit an initial peak of a similar magnitude for all investigated strain rates and stabilize to the static stress plateau for each architecture. While the global amount of potential energy remains largely unchanged for all investigated rates, the amount of dissipation and kinetic energy demonstrates a non-linear increase from static deformation to slow and high rate deformation. The phenomena observed in different architectures are highlighted, and the differences are explained and related back to the configurations of the lattices. Notably, the prevalent notion in literature asserting the superiority of negative Poisson's ratio materials for impact mitigation applications is not replicated in this study.

1. Introduction

The engineered microstructure of architected materials achieving unusual mechanical properties, resulting in so-called mechanical metamaterials, presents new opportunities for designers and engineers and new challenges for researchers [1–3]. Of particular interest is the design of metamaterials for impact mitigation. Impact events, necessitating protective measures, exist in a wide range of fields, from sports [4] over space travel [5], metal roofs in hailstorms [6], collisions between cars and civil infrastructure [7] to personal protective equipment [8]. In all these applications, the aim of the protective structure is to limit the energy and impulse transmitted from the impactor to the protected structure, be it a living being or an otherwise fragile material.

In this quest, auxetic (negative Poisson's ratio) materials have gained considerable interest in the research community in recent years, as evidenced by the reviews [9–12]. The negative Poisson's ratio, which characterizes auxetic materials, leads to lateral material contraction under compression, as shown in Fig. 1.1. For impact mitigation, auxetic materials are of special interest due to reported higher indentation resistance [13] as well as shear resistance [14]. Other promising properties for impact mitigation include increased fracture toughness [15] and enhanced energy absorption [16]. Auxetic materials naturally compress themselves underneath the impacted area, reportedly allowing for more mass-efficient protective solutions. However, these assumptions are based on homogeneous, isotropic materials under infinitesimal, quasi-static deformation. Whilst the majority of research investigating the applicability of auxetic structures for impact mitigation merely compares auxetic structures amongst each other or only report the properties of a single auxetic structure (e.g. [17–21]),

* Corresponding author at: Faculty of Civil Engineering and Geosciences, Delft University of Technology, Stevingweg 1, 2628 CN Delft, The Netherlands.
E-mail address: t.gartner@tudelft.nl (T. Gärtner).

https://doi.org/10.1016/j.mtadv.2025.100656
Received 3 September 2025; Received in revised form 22 October 2025; Accepted 3 November 2025

there are a few studies that compare auxetic with regular honeycomb structures [22–24]. However, to the best knowledge of the authors, there is no study which compares structures with comparable mass and stiffness. Farshbaf et al. [24] compare an auxetic with a conventional honeycomb unit cell, by folding the beams inwards without correcting for the reduced volume, resulting in a denser and stiffer auxetic unit cell and only evaluating the absolute energy absorption without normalizing it for the mass. Liu et al. [22] compare auxetic and conventional honeycomb in the same manner, leading to the same issue of unit cells of different masses and stiffnesses. Qi et al. [23] compare an auxetic honeycomb panel with a conventional honeycomb panel without specifying the properties of the conventional honeycomb panel beyond having "the same size, areal density and material as the re-entrant auxetic honeycomb panel". The same density mitigates the use of the absolute energy absorption as comparative measure, but gives no information on the expected stiffness of the panel. In the present study, we use the unit cells designed in our earlier contribution to show the same stiffness and relative density [25], to allow for a fair comparison between different unit cell designs and to eliminate these factors in our comparison.

As no relevant natural auxetic materials exist, this negative Poisson effect needs to be artificially created through mechanical metamaterials. Whilst mechanical metamaterials can be constructed from shells [26], plates [18,27], or as foams [28], the focus in this work is on auxetic structures based on structured beam-lattices. These architected materials are inherently *not* isotropic and, as they also undergo large deformations, their material properties vary throughout deformation. In beam lattices, the individual beams are re-oriented, leading to a change in the effective material properties [25].

As shown in [29] not only the pure energy absorption capability of a structure is of importance for impact mitigation, but also the — temporal and spatial — distribution of forces. In the present contribution, further investigation is conducted into the distribution of energy dissipation within the structure at varying strain rates for different refinement levels, alongside the subsequent effects on the force transmission from the impactor to the protected structure.

The investigation into the energy absorption of protective structures has thus far focused mostly on the energy dissipated by compression of the structure, and its conclusions focus on the higher amount of energy dissipated by auxetic lattices [22,23]. However, little attention is given to the internal mechanisms and the distribution of the energies in comparable metamaterials of different architectures, as well as the strain rate dependence in the response of different material architectures. Investigations of different collapse patterns under high speed compression were undertaken as early as the 1980s [30], where a comparison between two types of structures — one "O-type" with a static response akin to ideal plasticity and one "double I-type" with a static response showing significant softening — and their internal collapse mechanism is shown. Ruan et al. [31] investigated different modes of collapse occurring throughout different speeds in non-auxetic conventional honeycombs with different wall-thicknesses, showing the transition from nearly static, barrelling deformation modes to dynamically dominated, localized deformation in conventional honeycomb patches. More recently, investigations into the static mechanisms in the deformation of metamaterials, either driven by the boundary conditions [32] or by the interaction between local and global collapse patterns [33] have been conducted. However, only one type of fundamental architecture was investigated in all these works, and a comparison between different auxetic and non-auxetic architectures is yet to be made. The link between the collapse patterns, dynamic loading and the corresponding force transmission for different types of unit cells is explored in this manuscript. This study especially explores the resulting strain rate sensitivity of different architectures. To provide a first insight into this topic, numerical experiments are conducted using beam-based finite element analyses. For these analyses, three different fundamental unit cells, are investigated: **(a)** the most common auxetic type, a re-entrant honeycomb (cf. [34]); **(b)** an auxetic cell based on a rotation mechanism, the so-called missing ribs or chiral unit cell (cf. [35]); and **(c)** a non-auxetic unit cell, the regular honeycomb. The three unit cells are designed to exhibit the same relative density as well as initial stiffness (cf. [25]). Knowledge of the behaviour of these architectures will allow for better insight into the mechanisms of collapse under different strain rates and subsequent design studies to explore the applicability for impact mitigation. Here, special attention will be paid to the effects of microstructural refinement and transmission of forces from the strike face of the protective layer, i.e. the side of the structure subjected to the impact, to its back face, i.e. the interface with the opposing structure. This enables design engineers to decide on a protection concept fit for the expected impact events.

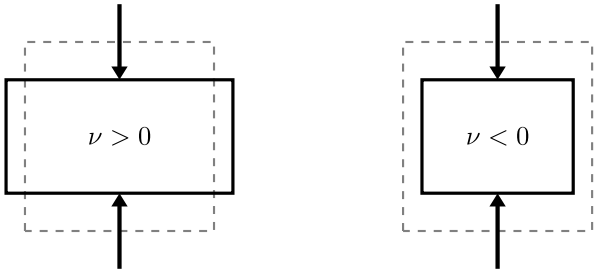

Fig. 1.1. Auxetic materials concept.

The architecture designs for the investigated metamaterials are presented in Section 2, and in Section 3 the numerical framework to conduct the investigation is laid out. In Section 4, an investigation into the static behaviour of different sizes of unit cells in a patch is presented, which forms the basis for the investigation into the force transmission at different rates through the patch in Section 5. To understand the processes involved in this force transmission better and obtain insight into the deformation patterns, in Section 6, the distribution of energies is presented and discussed. The article closes in Section 7 with a short discussion of the obtained results, limitations of this study and recommendations for further research.

2. Investigated architectures

The material of which the architectures are constructed from is taken to be a steel with a Young's modulus of 210 GPa, a Poisson's ratio of 0.3, and a density of $7850\,\mathrm{kg\,m^{-3}}$. All architectures investigated are designed to exhibit a Young's modulus of 300 MPa in vertical direction and a relative density with regard to the base material of 0.1. We continue to use the same architectures, that were derived in our earlier contribution [25]. During this design process, 2 or 3 independent measures (dependent on the particular architecture, as indicated in Figs. 2.1–2.3) are chosen that define each architecture. These independent variables are then optimized to achieve a design for each architecture that exhibits the same linear elastic target properties—relative density and vertical Young's modulus. An in-depth discussion on the static, elastic properties of these architectures, as well as the design process, can be found in [25]. It should, however, be noted that the absolute dimensions of the unit cells do not matter for the determination of the Young's modulus or the relative density, so that the unit cell can be directly scaled to the desired measures for the investigations conducted in this work.

The first investigated unit cell is the most common auxetic architecture, the re-entrant honeycomb (cf. [34]). Its configuration is shown in Fig. 2.1. The horizontal beam has a length of 100 mm, the tilted beams a length of 42.6 mm and the angle between the titled beams and the horizontal is set to be 65.6°. The beams itself have a square cross-section with a side length of 3.45 mm. Square beams are chosen to better

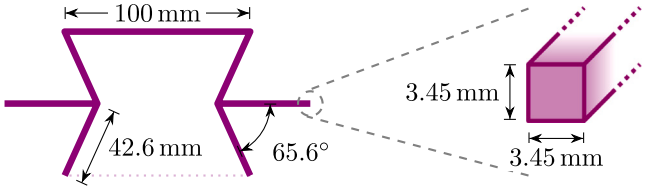

Fig. 2.1. Re-entrant unit cell used throughout this investigation.

represent a prismatic, 2.5-dimensional structure, and to allow for a fair comparison of the stresses reached for all investigated architectures.

In order to also capture unit cells with a fundamentally different deformation mechanism, chiral, sometimes called missing ribs, unit cells (cf. [35]) are investigated. Whilst the Poisson effect of re-entrant honeycombs is driven largely by inwards folding, the deformation of chiral unit cells is driven by rotation of the joints, resulting in a mechanism that can also be found in rotating squares unit cells (e.g. [32]). The chiral unit cell is depicted in Fig. 2.2. The length of a single beam in the centre is 75 mm and the angle between the horizontal (or vertical) axis and the beams is set to 28.1°. This results in a width of the entire unit cell of 132 mm and together with a square cross-section of 5.83 mm side length, the relative density of 0.1 and the effective Young's modulus of 300 MPa in vertical direction are obtained as for the re-entrant unit cell.

The final investigated unit cell is the non-auxetic honeycomb as depicted in Fig. 2.3. The horizontal beam has a length of 75 mm and the tilted beams are 85.4 mm long. The beams have a square cross-section with a side length of 7.08 mm and the angle between the tilted beams and the horizontal is set to 119.7°. Again, the resulting Young's modulus and relative density are 300 MPa in vertical direction and 0.1, respectively.

All three unit cells are subsequently assembled into patches. When assembling these patches, the unit cells are scaled down, to ensure that the overall patch has the same outer dimensions for each architecture. For the scaling, all geometric dimensions, the length of the beams, as well as the dimensions of their cross-sections are scaled by the same factor. The thickness in the third direction is thus changing for a different number of unit cells, which is accounted for in the later analyses. A comparison between two patches consisting of 2×2 and 12×12 unit cells is shown in Fig. 2.4. In this illustration, the scaling of the singular unit cells to achieve the same outer dimension is shown.

3. Numerical framework

The implementation for this work uses the JIVE-Framework [36].

In order to model patches made from the unit cells described above, the lattices are subsequently modelled as a collection of nonlinear Timoshenko-Ehrenfest beams. These beams are also called special Cosserat rods, geometrically exact beams or Simo-Reissner beams after [37,38]. Such beams can be described by the position of their centreline and the orientation of the cross-sections along the centreline. The resulting six-dimensional space of strain-prescriptors corresponds with a six-dimensional space of stress-resultants. It should be noted here, that all out-of-plane degrees of freedom — displacement in out-of-plane direction, as well as rotation around the in-plane axes — are constrained, resulting essentially in a two-dimensional beam model. Therefore, for the sake of brevity, in the following only the parameters relevant to in-plane deformation are reported.

For the initial, elastic response of the beams, a linear elastic relation between the stress-resultant forces and moment and the elastic strain-prescriptors is assumed:

$$\begin{bmatrix} N_1 \\ N_3 \\ M_2 \end{bmatrix} = \begin{bmatrix} kGA & 0 & 0 \\ 0 & EA & 0 \\ 0 & 0 & EI \end{bmatrix} \cdot \left(\begin{bmatrix} \Gamma_1 \\ \Gamma_3 \\ \mathcal{K}_2 \end{bmatrix} - \begin{bmatrix} \Gamma_1 \\ \Gamma_3 \\ \mathcal{K}_2 \end{bmatrix}_p \right), \tag{1}$$

Table 1
Material parameters of the base material of the lattice.

Name	Symbol	Value
Young's Modulus	E	210 GPa
Poisson's Ratio	ν	0.3
Shear Correction	k	$\frac{5}{6}$
Density	ϱ	7850 kg m^{-3}
Yield stress	σ_y	280 MPa
Hardening modulus	h	1750 MPa

with the stress resultant N_1 representing the shear force, N_3 the axial force, and M_2 the bending moment, expressed in the material frame of reference. The elastic strain prescriptors are computed from the total strain prescriptors and the plastic state $(\cdot_p)$. Here the shear strain is represented by Γ_1, the axial elongation by Γ_3 and the bending curvature by $\mathcal{K}_2$. For plastic material behaviour of the beam, a direct approach is used incorporating plasticity into the beam-level variables as discussed in [39,40]. The yield function Φ for a reference quadratic cross-section of side length 0.75 mm is taken to be

$$\Phi = \left| \frac{N_1}{71.8\,\mathrm{N} - N_1^h} \right|^{2.68} + \left| \frac{N_3}{164\,\mathrm{N} - N_3^h} \right|^{1.75} + \left| \frac{M_2}{30.8\,\mathrm{N\,mm} - M_2^h} \right|^{1.93} - 1. \tag{2}$$

We arrive at these numerical values by scaling values derived by Herrnböck et al. [41] for a J2-plasticity model with isotropic hardening at a yield limit of $\sigma_y = 450$ MPa and scaling them down linearly to the yield limit of our material model (cf. Table 1 and [29]) and then scaling each component individually according to the procedures laid out [41]. In order to arrive at consistent scaling for the yield surface in the stress resultant space of a beam, the yield forces need to be scaled with the length squared and the yield moments with the length to the power of three [41]. In order to capture the hardening behaviour of the material, we follow again the approach of [39]. It should be noted here, that isotropic hardening on material level results in kinematic hardening on beam level (cf. [42]). The kinematic hardening values derived by [42] and using the scaling approach suggested by [40] results for a reference cross-section of side length 0.75 mm in the hardening tensor

$$\boldsymbol{H} = \begin{bmatrix} 936\,\mathrm{N} & 1630\,\mathrm{N} & 618\,\mathrm{N\,mm} \\ & 2800\,\mathrm{N} & 907\,\mathrm{N\,mm} \\ \text{sym.} & & 443\,\mathrm{N\,mm^2} \end{bmatrix}. \tag{3}$$

To arrive at the numerical values for this hardening tensor we first scale the values described by [42] for a hardening modulus of $h = 20\,000$ MPa linearly to the assumed hardening modulus of $h = 1750$ MPa. Subsequently, each value is scaled according to the strategy in [40], i.e. the translational parts of the hardening tensor are scaled with the length squared, the rotational parts with the length to the power of four and the coupling parts with the length to the power of three. For a deeper treatise, the reader is referred to [39,40,42].

It should be noted here, that these are merely the values for the reference cross-section — a square with side length 0.75 mm — and the parameters need to be scaled for every simulation run in accordance with the strategies provided by [40,41]. The employed parameters were originally derived in a previous study into the impact behaviour of architected materials [29]. In this study also a comparison of the employed model with ballistic experiments as well as commercial FE software was undertaken, and the parameters were deemed to be sufficiently accurate to be able to predict the deformation and force transmission behaviour of the investigated lattice structures [29].

The approach of Simo and Vu-Quoc [43] and subsequent improvements proposed by Crisfield and Jelenić [44] are followed to determine the global stiffness matrix and resulting nodal forces. As we are using an explicit return mapping scheme we employ the elastic stiffness matrix throughout the analysis irrespective of the plastic deformation present throughout the beam. During the simulation, beams are discretized

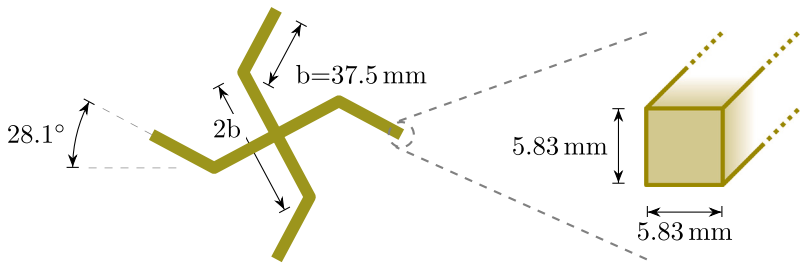

Fig. 2.2. Chiral unit cell used throughout this investigation.

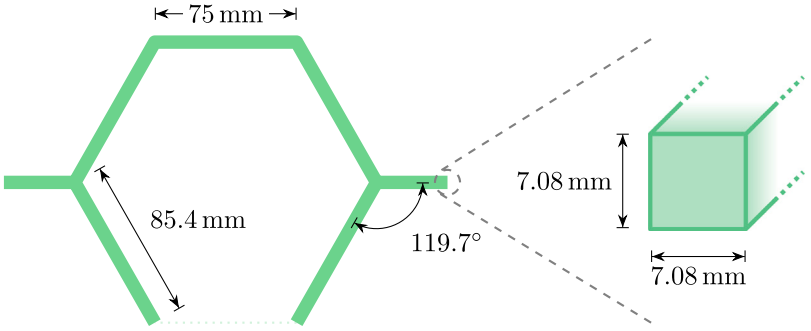

Fig. 2.3. Honeycomb unit cell used throughout this investigation.

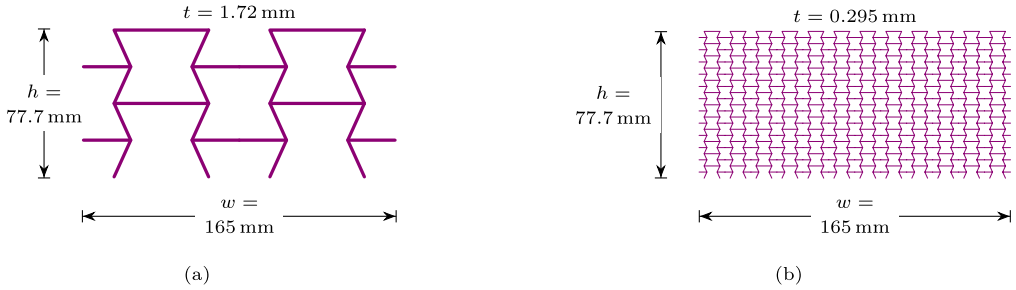

Fig. 2.4. Patches from 2×2 and 12×12 unit cells, scaled to ensure the same outer dimensions.

using linear elements with Lagrangian shape functions and uniformly reduced integration to avoid shear-locking phenomena.

Contact between the beams is implemented following [45]. We assume frictionless contact between two linear two-node elements. For each node-to-element pairing the contact forces are computed using a penalty approach. In order to scale the contact stiffness with the size of the contact points, the penalty parameter ϵ is adapted with the square of the thickness of the beams t

$$\epsilon = 1 \times 10^7 \cdot \left(\frac{t}{1\,\text{mm}}\right)^2. \tag{4}$$

This scaling is motivated by comparison of the contact forces added by the penalty approach and the internal forces within each beam, which are scaled with the cross-sectional area of the beam (compare also the force parts in Eq. (1)). In order to ensure consistent scaling of all forces in the model, the penalty parameter, which translates to the level of the contact forces, is scaled similarly. Additionally, as the contact is not between the centrelines of the beams directly, contact radii around all beams are introduced and set to half the beam thickness

$$r = \frac{t}{2}. \tag{5}$$

For the static investigations an implicit Newton–Raphson scheme is employed, whilst the dynamic investigations are computed using an explicit scheme with adaptive time stepping. This adaptive stepping scheme uses an explicit and implicit Euler scheme as a predictor–corrector pair and a Milne-device [46] as error estimator. The orientation matrices, being of the special orthogonal group SO(3), are integrated using an exponential integrator (e.g. [47]).

This complete model allows to capture the relevant non-linearities present in an impact scenario. It represents an accurate approach for the large, inelastic deformations, including contact, present in a typical impact scenario, as shown in earlier comparison with experimental data and commercial FE solutions [29].

Throughout the analysis, different stress and energy measures are recorded. The stress on the strike face is the sum of the resulting nodal forces in vertical direction on the top boundary divided by the width of the sample w and the thickness t of a beam. A similar computation is employed for the back face. As the resulting forces on the strike face are typically acting downwards (in negative direction) a factor of -1 is added to obtain positive values:

$$\sigma_{\text{strike}} = -1 \cdot \frac{\sum f_{\text{strike}}}{wt}, \tag{6}$$

$$\sigma_{\text{back}} = \frac{\sum f_{\text{back}}}{wt}. \tag{7}$$

The SEA, i.e. the external work put into the system, is calculated by integrating the sum of the resulting forces on the strike face over the displacement of the strike face u_{strike} and normalizing it by the mass of

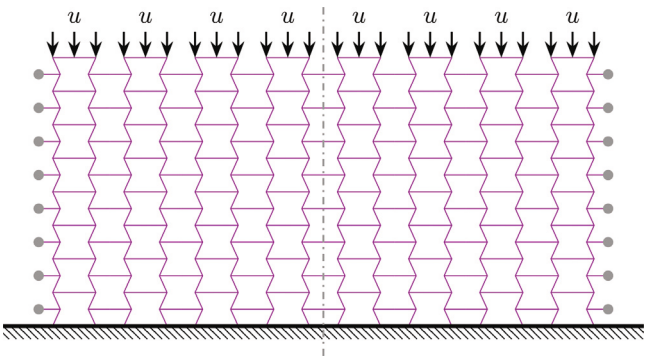

Fig. 3.1. Boundary conditions applied in this investigation at the example of an 8×8 patch.

the patch m_{patch}:

$$\text{SEA}(u) = \frac{1}{m_{\text{patch}}} \int_0^u \left(\sum f_{\text{strike}} \right) \mathrm{d}u_{\text{strike}}, \tag{8}$$

where the integration is executed using the discrete values recorded during the simulation using Simpson's rule. The potential, kinetic and dissipated energies are recorded on a nodal basis. The kinetic energy is directly computed from the nodal velocities and the global mass matrix, whereas the potential and dissipated energies are calculated per element and subsequently integrated for each node using standard finite element procedures.

As the time-steps for the different simulations are not identical, and the dynamic simulations conducted show high-frequency oscillations due to the absence of damping in the model, all reported measures are created from the average of bins stretching 0.5 % compression each. E.g. the point plotted at 15 % compression is the average of the recorded values between 14.75 % and 15.25 % compression.

3.1. Boundary conditions

In order to estimate the behaviour of different patch configurations, a set of boundary conditions mimicking a constant strain-rate setup is applied. This will allow for an initial estimation of the differences in strain rate dependence among the various architectures. Future studies are then enabled to tailor specific protection concepts to expected threat levels. An overview of these boundary conditions can be found in Fig. 3.1. On the bottom side, the patch is fully fixed, whilst at the top side, horizontal movement is prevented and a vertical, compressive displacement $u = u_{\text{strike}}$ is enforced. The boundary nodes on the left and on the right side are enforced to deform symmetrically with respect to a symmetry plane corresponding to the centre of the patch, in order to prevent globally asymmetric deformation.

Throughout this study, different compression rates $\dot{u}/h$ are investigated. As a reference case *static* compression is analysed. For the dynamic investigations, the investigated strain rates are $\dot{u}/h = 250\,\text{s}^{-1}$, $\dot{u}/h = 1000\,\text{s}^{-1}$, and $\dot{u}/h = 4000\,\text{s}^{-1}$. These rates will be called in the remainder of the manuscript *slow* rate compression ($\dot{u}/h = 250\,\text{s}^{-1}$), *medium* rate compression ($\dot{u}/h = 1000\,\text{s}^{-1}$), and *fast* rate compression ($\dot{u}/h = 4000\,\text{s}^{-1}$).

4. Effects of the number of unit cells

As a first investigation, using the boundary conditions described above, the effect of the number of unit cells within the patch is analysed. For this, unit cells of different size are assembled into patches of the same overall size, ensuring the same elastic tangent properties, as explained in Section 2 and shown in Fig. 2.4. This scaling results in e.g. each individual unit cell in a 2×2 patch to be twice as high and wide as each individual unit cell in a 4×4 patch. The resulting changes in the thickness of the patch in the third dimension t are explicitly accounted for when calculating the stresses in Eqs. (6) and (7) and implicitly via the total mass m_{patch} when calculating the SEA in Eq. (8).

4.1. Re-entrant unit cells

The behaviour of different re-entrant patches under *static* compression is investigated first. In Fig. 4.1 the *static* stress–strain curves at the strike face for different numbers of re-entrant unit cells under compression are shown. All investigated patches show onset of plasticity at 1 % compression. Prior to the onset of plasticity, there is some loss of stiffness corresponding with the re-orientation of beams and the subsequent shift in load-carrying capacity as discussed in [25]. After the onset of plasticity, as the load carrying capacity of the beams is limited at yield, nearly no stiffness remains upon further deformation. When the unit cell size is decreased, a more brittle response is observed. This phenomenon is attributed to the more pronounced localization resulting from the smaller unit cells, and thus in less material undergoing large deformations. The hardening in later stages of the response, most clearly seen for the 12×12 patch, is an effect of contact within the unit cells.

The deformation patterns in Fig. 4.2 support this observation. In this figure, the deformed configurations of 4×4, 8×8, and 12×12 unit cell patches are showcased for 1 %, 10 % and 20 % compression. These compression levels are indicated by vertical lines in Fig. 4.1 as well. Here, it can be seen, that 1 % compression coincides with the loss of stiffness due to plasticity. During the initial, mostly elastic deformation (depicted in the top row), the patches are deformed uniformly. At a deformation of 10 %, differences in deformation are visible: Whereas in the 4×4 and the 8×8 patch, on the left and in the centre, the deformation appears symmetric both along the vertical axis as well the horizontal axis, the 12×12 patch on the right side of the figure shows a break of symmetry along the horizontal axis, i.e. the deformation of the top half does not mirror the deformation of the bottom half. This is due to a localization of deformation near the bottom edge. A stronger deformation within a single row of unit cells leads to a stronger loss in stiffness and a more brittle response. Once such a weak spot appears, the remaining deformation concentrates around it. In the last row of Fig. 4.2, the deformation state for 20 % compression is shown. Here, the localization is intensified and becomes visible for the 8×8 unit cell patch in the centre of the figure as well, whilst the 4×4 patch on the left maintains both symmetries. All investigated patches suffer from loss of convergence in the global Newton–Raphson scheme at different stages of compression. The common cause of these numerical problems is the contact between free ends of beams at the left and right boundaries of the patch, as can be seen for example in the centre of the 4×4 unit cell patch at both sides between the second and third unit cell. This loss of convergence is limited to the static, implicit analysis and is, as it does not occur in the explicit, dynamic scheme, deemed acceptable.

For the investigations of the impact behaviour of architected metamaterials, the consideration of dynamic deformation is of crucial importance. To this end, the effects of different numbers of unit cells on the dynamic response of a patch are investigated as well. In Fig. 4.3 the stress–strain curves measured at the strike face for *fast* rate compression are shown. For all patches, an initial rise in the stress can be observed, followed by a loss in stiffness, that is occurring earlier for smaller unit cells. Prior to the onset of plasticity at around 1 %, smaller unit cells show a more stiff response, attributed to differences in the distribution of inertia within the patches. After this, smaller unit cells show a more brittle behaviour, as already seen for the *static* case in Fig. 4.1. For a better understanding of the dynamic behaviour of the different patches, again, 4×4, 8×8, and 12×12 unit cell patches are shown at 6 %, 12 % and 24 % compression in Fig. 4.4. As can be seen in the higher stress levels in Fig. 4.3 compared with Fig. 4.1 and the concentration of the deformation near the moving boundary in the patches in Fig. 4.4, the response is driven by inertia and not by the

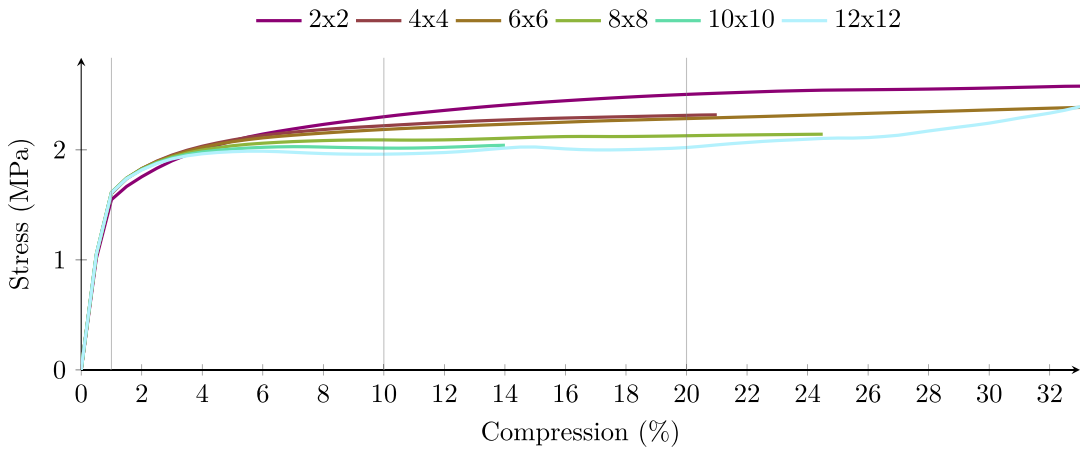

Fig. 4.1. Stress–strain curves of patches with a different number of re-entrant unit cells under *static* compression.

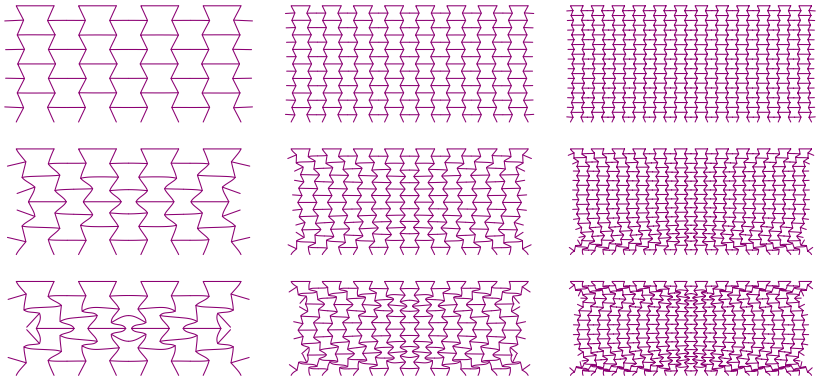

Fig. 4.2. Re-entrant 4×4 (left), 8×8 (centre), and 12×12 (right) unit cell patches under *static* deformation at 1 %, 10 % and 20 % compression.

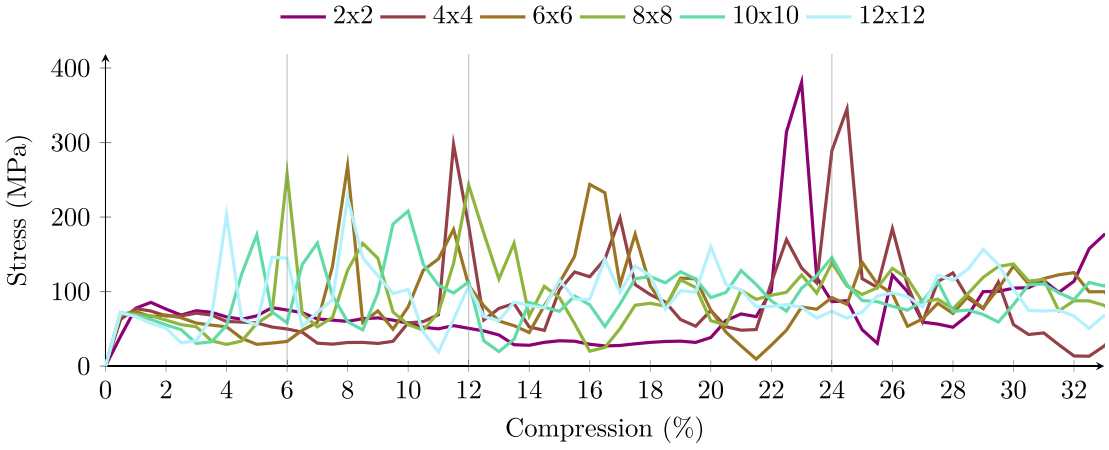

Fig. 4.3. Stress–strain curves of patches with a different number of re-entrant unit cells under *fast* rate compression.

structural response. This is due to the fact that the accelerating forces are beyond the yield limit of the upper parts of the structure. These forces lead to a localized collapse of the structure near the strike face. The peaks observed throughout the stress–strain curves in Fig. 4.3 put further emphasis on this observation. 6 % compression corresponds with the first peak for the 8×8 unit cell patch, as indicated by the thin vertical line in Fig. 4.3. At this compression level, it can be seen from the first row of Fig. 4.4 in the centre column that the first half unit cell is fully collapsed and the corresponding horizontal row of beams starts to come into contact. The acceleration of this horizontal row of beams is the explanation for the increased stress experienced at the strike face. The size of half a unit cell in horizontal direction would correspond to 6.25 % of the length for an 8×8 patch. The effect occurs already at lower compression levels due to the finite sized beams coming into contact already earlier and plotting methodology averaging the stresses over 0.5 % compression.

At 12 % compression, showcased in the centre row of Fig. 4.4, first contact can be seen for the 4×4 patch as well as contact with the second row of horizontal beams for the 8×8 patch. This corresponds well with the peaks in Fig. 4.3. This observation provides a rationale for the earlier occurrence of peaks in the stress response for a smaller unit cell size. After a nominal compression of 24 %, in the lower row of

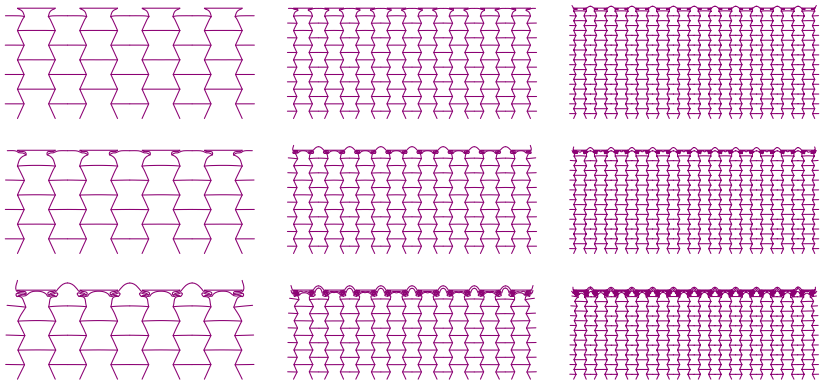

Fig. 4.4. Re-entrant 4 × 4 (left), 8 × 8 (centre), and 12 × 12 (right) unit cell patches under *fast* rate deformation at 6 %, 12 % and 24 % compression.

Fig. 4.4, all deformation is concentrated at the top and the lower parts do not show any deformation. One should note here, that the bulging of the beams through the upper boundary is not an error, but a limitation of the employed boundary conditions only constraining the nodes at the top boundary in the undeformed configuration. The limitation is acceptable as the bulging elements are not causing numerical issues and are connected to the rest of the lattice. Furthermore, they are sufficiently far from the bottom boundary, which is the focus of the remaining investigations. The remaining stress–strain curves for *slow* and *medium* compression as well as the corresponding deformation patterns are shown in Appendix A.1.

4.2. Chiral unit cells

Next to the re-entrant unit cell, the behaviour of patches from chiral unit cells is analysed. The *static* stress–strain curves are shown in Fig. 4.5. Also for this architecture, in these curves the onset of plasticity can be seen at 1 %. Similar to the re-entrant patches in Fig. 4.1, all structures initially show a hardening response. This hardening response is then followed by a softening response, which is more pronounced for smaller unit cells. This is consistent with earlier observed tendencies, that smaller unit cells lead to an earlier and stronger localization of the deformation. The deformed configurations for 4 × 4, 8 × 8, and 12 × 12 patches at 5 %, 10 % and 20 % are visualized in Fig. 4.6. These compression levels are marked in Fig. 4.5 by thin vertical lines. In the stress–strain curves, it can be seen, that at 5 % compression both the 4×4 on the left and 8×8 patches in the centre are still in the first hardening phase, whilst the 12 × 12 patch on the right is already in the softening phase. Upon inspection of the deformation patterns, it can be seen, that the 12 × 12 patch exhibits localizations of deformation (near the top of the patch), whilst the other two still showcase uniform deformation. At 10 % compression, the 12 × 12 patch on the right side of the figure shows contact, leading to a slightly stiffer response. The 8 × 8 patch in the centre has also entered the softening phase and showcases clearly localized deformation as well. The 4 × 4 patch on the left is near the peak of its stress level and when examining the deformation patterns, the start of localized deformation can be seen as well. At the last investigated compression level of 20 %, the 8 × 8 patch shows multiple points of internal contact, which corresponds to the global hardening of the patch. On the other hand, the 4 × 4 patch shows no contact yet, which is consistent with the ongoing softening behaviour of the overall patch as seen in Fig. 4.5. After further deformation, beams within the patch will come into contact, marking the transition from the softening phase to the re-hardening phase. It should be noted, that chiral patches show strong local asymmetries in their behaviour despite the enforced global symmetry, due to the rotating mechanism responsible for the negative Poisson effect. For the chiral unit cells, as is the case for the re-entrant ones, the static solution scheme suffers from loss of convergence after a larger number of beams or the free ends of beams come into contact.

The dynamic behaviour is investigated for the chiral unit cells as well and the resulting stress–strain curves for *fast* compression are shown in Fig. 4.7. An initial maximum appears around the onset of plasticity at 1 % deformation. Here, as is the case for re-entrant patches, smaller unit cells show a stiffer response not seen in static deformation, attributed again to differences in the distribution of inertia within the patches. Furthermore, smaller unit cells show a more brittle response after the first peak around 1 % compression, as seen earlier for the re-entrant unit cells in Fig. 4.3, consistent with the *static* behaviour of both auxetic unit cells. Afterwards all investigated patches show further peaks, appearing later for larger unit cells, i.e. patches with a smaller number of unit cells. In order to understand the reason behind these peaks, the deformed patches are plotted for 6 %, 12 % and 24 % compression and shown in Fig. 4.8. All patches show a clear localization of the deformation at the top and no deformation of the remaining parts of the structure. At 6 % deformation, for the 8 × 8 patch, half a unit cell is compressed, and contact between the upper nodes as well as the next horizontal row of beams is achieved. The acceleration of these beams corresponds with a peak in the stress–strain curve seen in Fig. 4.7. The same phenomenon can be seen in the 4 × 4 patch at 12 % deformation, both in the deformation plots in Fig. 4.8 and the stress–strain curve in Fig. 4.7. The peaks are cut off in the figure for better visibility, but larger elements show peaks of higher magnitude, i.e. from the peak for 12 × 12 unit cells at about 800 MPa the stress level rises over approximately 2000 MPa for 6 × 6 unit cells to roughly 6000 MPa for the 2 × 2 unit cell patch. These phenomena are similar to the ones observed in the re-entrant patch. Additional stress–strain curves for *slow* and *medium* compression as well as the corresponding deformation patterns are shown in Appendix A.2.

4.3. Honeycomb unit cells

In order to make a comparison with the auxetic unit cells, regular honeycomb unit cell patches with a positive Poisson's ratio are investigated. The corresponding static stress–strain curves are shown in Fig. 4.9. We observe the same kink in the curve at the onset of plasticity as for the patches with re-entrant and chiral unit cells. For smaller unit cells neither the reduction in the hardening response, observed for the re-entrant architecture, nor earlier softening, as for the chiral architecture, is observed. This is also confirmed in the deformation patterns of 4 × 4, 8 × 8, and 12 × 12 unit cell patches in Fig. 4.10. Global barrelling is clearly visible for the 8 × 8 and 12 × 12 cases, in the centre and on the right side respectively. As the barrelling response is a global pattern we can, in Fig. 4.9, observe a convergence of the response already at smaller numbers of unit cells compared to the two investigated auxetic structures in Figs. 4.1 and 4.5, in which localized deformation is occurring.

For the dynamic investigation of different honeycomb patches, again the stress–strain curves under *fast* compression are examined, as

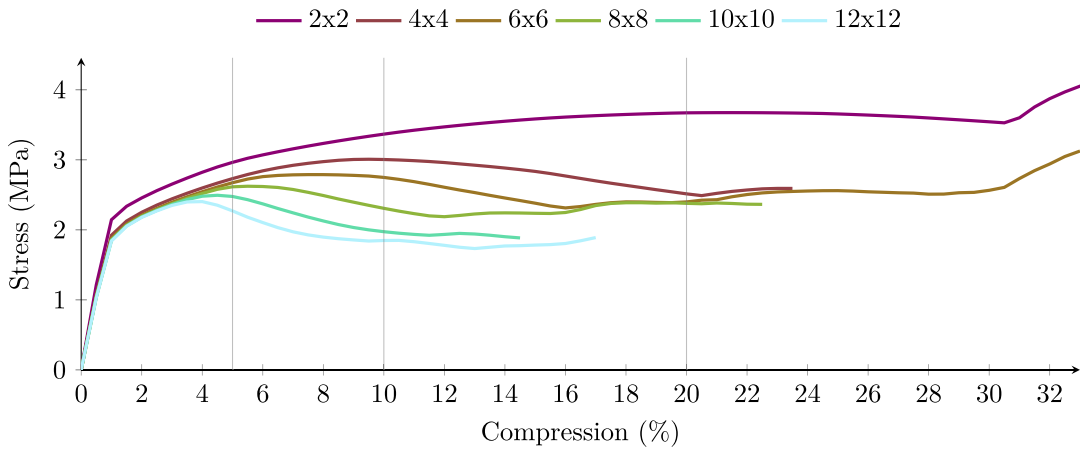

Fig. 4.5. Stress–strain curves of patches with a different number of chiral unit cells under *static* compression.

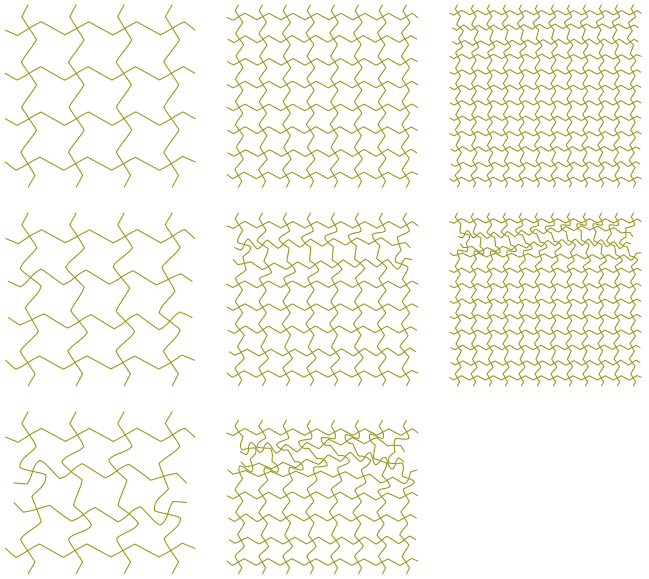

Fig. 4.6. Chiral 4×4 (left), 8×8 (centre), and 12×12 (right) unit cell patches under *static* deformation at 5 %, 10 % and 20 % compression.

shown in Fig. 4.11. The initial response, prior to the onset of plasticity at 1 % shows, opposed to the observations in static deformation, a stiffer response for smaller unit cells, motivated again by differences in the distribution of inertia for different sizes of unit cells. After this onset of plasticity, a more brittle response is observed for smaller unit cells, in agreement with the observations made for both auxetic architectures. In the stress–strain curves, peaks are seen at lower compression for smaller unit cells and at higher compression levels for larger unit cells as already seen in the responses of the two auxetic architectures. Nevertheless, fewer peaks are observed than for the two auxetic architectures. To illustrate the reason behind this, in Fig. 4.12, the deformed shapes of 4×4, 8×8, and 12×12 unit cell patches at compression levels of 6 %, 12 % and 24 % are shown. Whereas both auxetic structures show peaks in their stress response at a compression level of 6 %, this peak is not seen in the response of the non-auxetic patches. In the deformed shapes in Fig. 4.12, it can be seen, that none of the patches show any contact yet, as the beams at the upper boundary do not come into contact with the beams at half a unit cell height due to the convex structure of the honeycomb architecture. For this same reason, a full unit cell of compression is needed for the non-auxetic honeycomb structures to experience contact. At this point, shown in the centre row at 12 % compression for the 8×8 patch in the central columns and in the bottom row at 24 % compression for the 4×4 patch on the left side, contact is seen. This corresponds with the stress peaks in Fig. 4.11, where the first peak for the 8×8 patch occurs at 12 % and the first peak of the 4×4 patch at 24 %. These values are again marked by thin vertical lines. For better readability of the graph, the peaks are again cut off but are rising from about 2000 MPa for the 12×12 patch up to about 4000 MPa for the 4×4 patch. The 2×2 unit cell patch does not show a peak in the first 33 % compression. The other stress–strain curves for *slow* and *medium* compression as well as the corresponding deformation patterns are shown in Appendix A.3.

4.4. Comparison of unit cells

Balancing the convergence behaviour in the *static* case, the dynamic behaviour and the computational cost, it is decided to take 8×8 unit cell patches as representative. Thus, 8×8 patches are used in the dynamic investigations in Sections 5 and 6 on force transmission and energy distribution.

A first comparison between 8×8 patches using the three architectures is shown in Fig. 4.13. In this figure, the stress–strain curves are shown for the investigated rates. During *static* compression, both investigated auxetic architectures, re-entrant and chiral, show a similar level of stress, whereas the honeycomb architecture not only shows a higher overall level, but also a significant hardening throughout the compression, leading to more than twice the amount of stress needed for compression. This difference is explained by the fundamentally different deformation modes in the patches: localized collapse in the case of the re-entrant and chiral architectures versus global barrelling in the case of the honeycomb. These deformation modes are consistent with the modes observed at quasi-static compression throughout literature [22,24,31]. Also for *slow* compression, the honeycomb shows roughly twice as high stress levels at the strike face compared to the auxetic architectures. As the *static* deformation patterns are less relevant at higher speeds, in the *medium* rate, peaks begin to appear, as discussed above. Here the re-entrant structure remains at a low stress level, and both the chiral and honeycomb patches show a large fluctuation of similar magnitude. This is even further emphasized for the *fast* rate, where the chiral and honeycomb structures again exhibit peaks of comparable magnitude, with the re-entrant patch remaining at a lower stress level, despite a few distinct peaks. The shift in deformation modes towards a concentration at the top of the compressed patch is in agreement with literature as well [22,31]. From this it can be concluded that in all loading scenarios, the honeycomb structure outperforms the auxetic ones regarding the stress needed to compress the patch to the same level, which is — for the static case — consistent with the results from other investigations [24]. For all

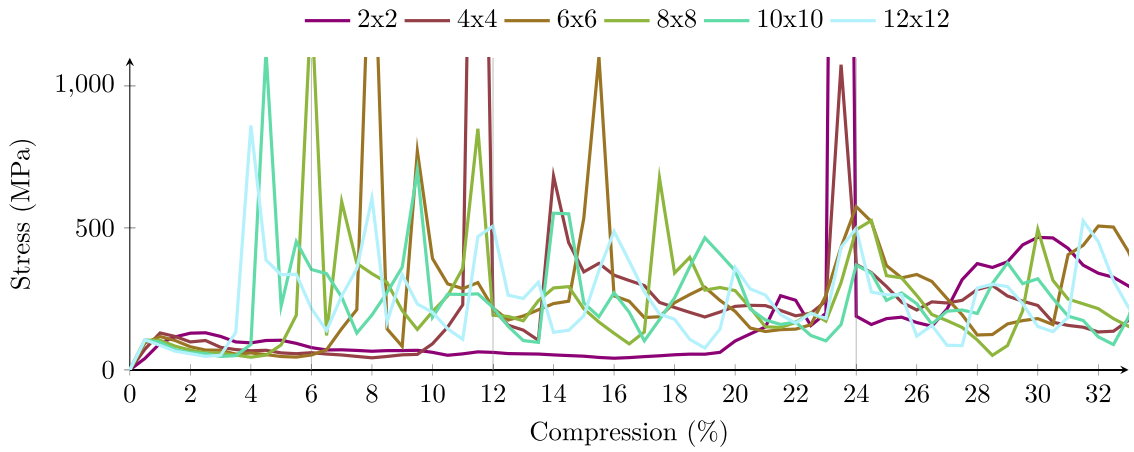

Fig. 4.7. Stress–strain curves of patches with a different number of chiral unit cells under *fast* rate compression.

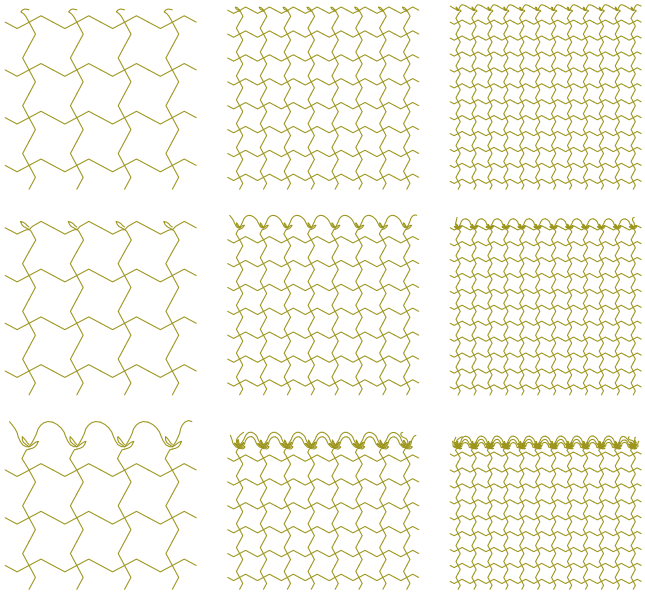

Fig. 4.8. Chiral 4×4 (left), 8×8 (centre), and 12×12 (right) unit cell patches under *fast* rate deformation at 6 %, 12 % and 24 % compression.

investigated architectures, whilst the *static* deformation modes differ and only the auxetic patches show localized deformation, during *fast* compression, the response is dominated by inertial effects, leading to a more brittle behaviour for smaller unit cells of all architectures, as discussed in the previous sections. Dynamic effects within the patches will be investigated in more detail in the following.

5. Effects of strain rate on the force transmission

In order to assess the efficacy of a protection concept, one not only needs to assess the forces exhibited at the strike face, but also the transmission of those forces through the protective layer, as was done in [29] for an emulated impact event with focus on the local distribution of these forces. The measurement of the forces acting on the strike face during an impact event has little information regarding the forces acting on the back face, thus the next investigation focuses on the transmission of forces from the strike face to the back face.

5.1. Re-entrant patch

To investigate this transmission of the force through the protective layer, a first comparison is done between the stresses on the strike face and the back face for the *slow* rate compression. The corresponding stresses, both on the strike face (the top boundary in Fig. 3.1) and on the back face (the bottom boundary in Fig. 3.1), are shown over the compression in Fig. 5.1. An additional abscissa is given depicting the time corresponding to the amount of compression at this strain rate. The stress on the back face follows the stress on the strike face with a delay, and both finally converge towards the same stress level. The magnitude of the delay, especially in the first rise of the stress, can be explained by the time needed for the elastic pressure wave to travel through the patch. Given the material parameters laid out in Section 3, the pressure wave speed through a beam is

$$c_{\text{metal}} = \sqrt{\frac{210\,\text{GPa}}{7850\,\text{kg m}^{-3}}} \approx 5172\,\text{m s}^{-1}. \tag{9}$$

Together with the height of the patch of $h = 77.7\,\text{mm}$ and the angle between the beams and the vertical of $\alpha = 24.4°$, the time required for the pressure wave to reach the bottom equals

$$t_{\text{metal}} = \frac{h/\cos(\alpha)}{c_{\text{metal}}} \approx 16.5\,\mu\text{s}. \tag{10}$$

This time is marked in Fig. 5.1 with a thin vertical line and corresponds with the first rise in stress being recorded at the back face.

The behaviour of the patch under *fast* rate compression is then investigated, and the resulting stresses recorded at the strike face and the back face are shown in Fig. 5.2. The stresses at the back face are of the order of 5 MPa, whereas the stresses on the front face are of the order of 100 MPa, indicating a reduction of the forces by more than an order of magnitude during the dynamic compression. The delay in the stress on the back face is again visible and corresponds with the time required for the stress wave through the metal t_{metal}. In this graph, the peaks in the stresses on the strike face at intervals of 6.25 %, corresponding to half the height of a unit cell, as discussed in Section 4 can be seen as well.

To compare different rates, in Fig. 5.3, the stresses on both faces are plotted for the investigated compression rates. On the strike face, we can observe an increase of the stresses needed to compress the patch at the given rates. This increase is moderate for *slow* and *medium* rate compression when compared to *static* compression, but increases significantly for *fast* rate compression. On the back face, it is clearly observed, that the stresses for both *slow* and *medium* rate compression approach *static* compression stress, despite the increase seen on the strike face.[1] For the *fast* compression case, this cannot be observed. The

[1] It should be noted here, that the employed material model does not consider strain rate sensitivity. If the base material itself shows strain rate sensitivity this would likely be reflected in the collapsing structure and lead to different stress levels for different rates.

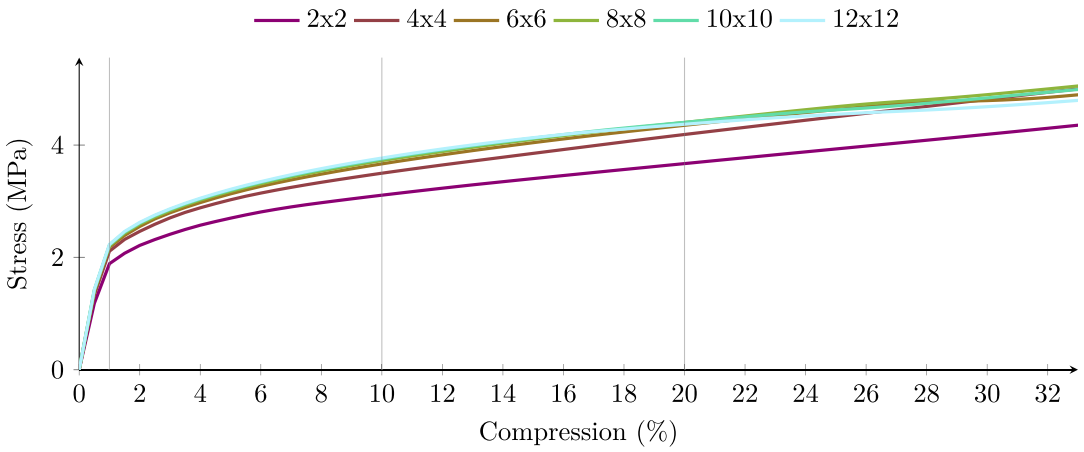

Fig. 4.9. Stress–strain curves of patches with a different number of honeycombs unit cells under *static* compression.

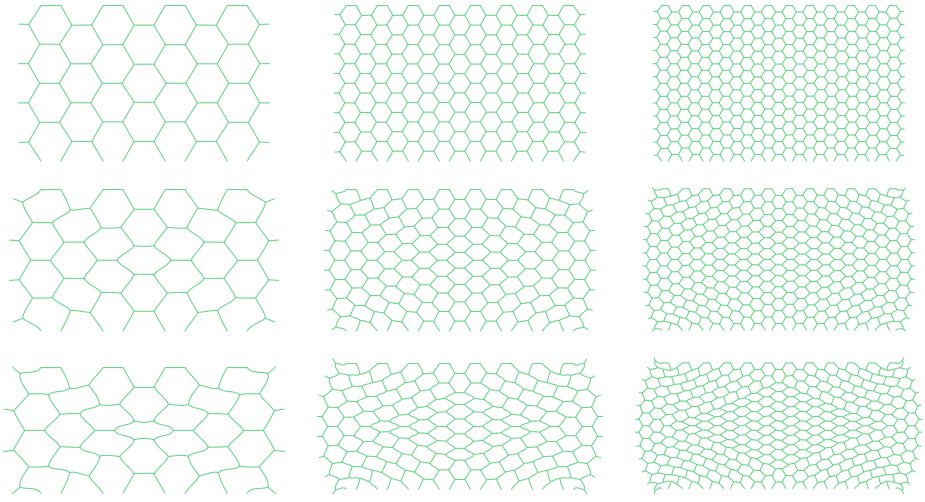

Fig. 4.10. 4×4 (left), 8×8 (centre), and 12×12 (right) unit cell patches under *static* deformation at 1 %, 10 % and 20 % compression.

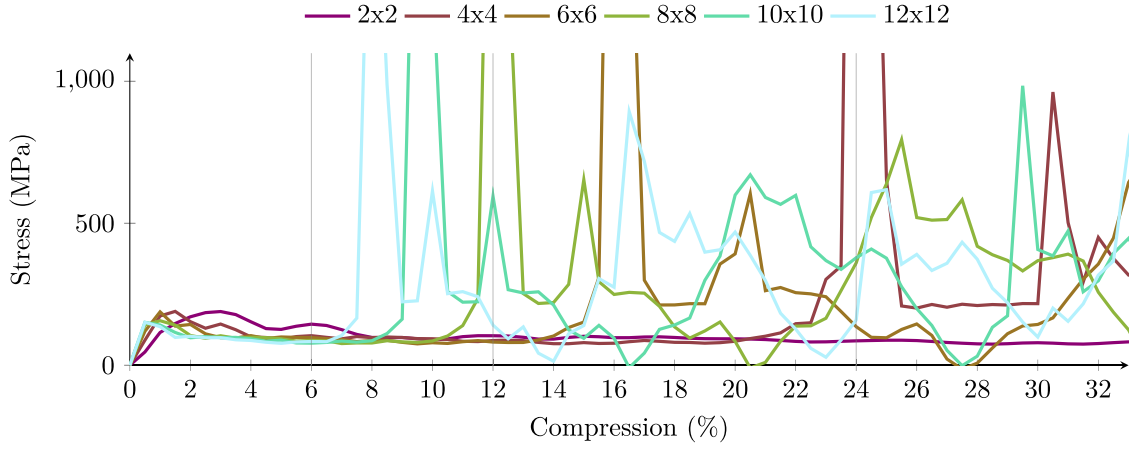

Fig. 4.11. Stress–strain curves of patches with a different number of honeycombs unit cells under *fast* rate compression.

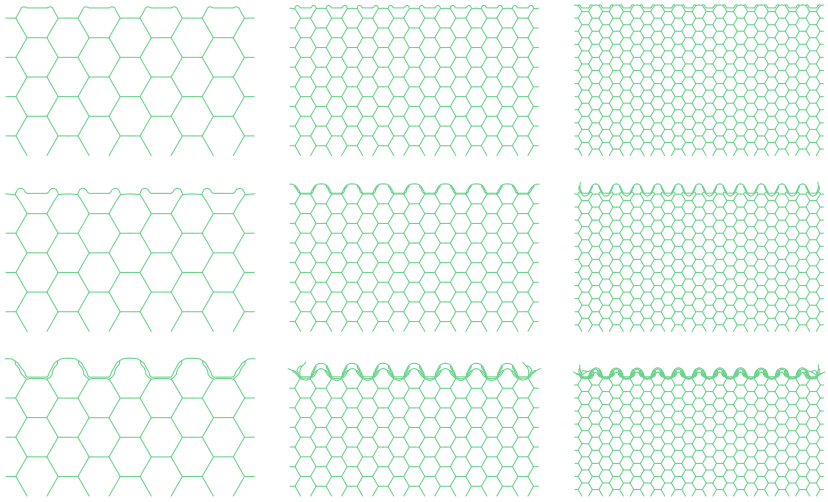

Fig. 4.12. 4×4 (left), 8×8 (centre), and 12×12 (right) unit cell patches under *fast* rate deformation at 6 %, 12 % and 24 % compression.

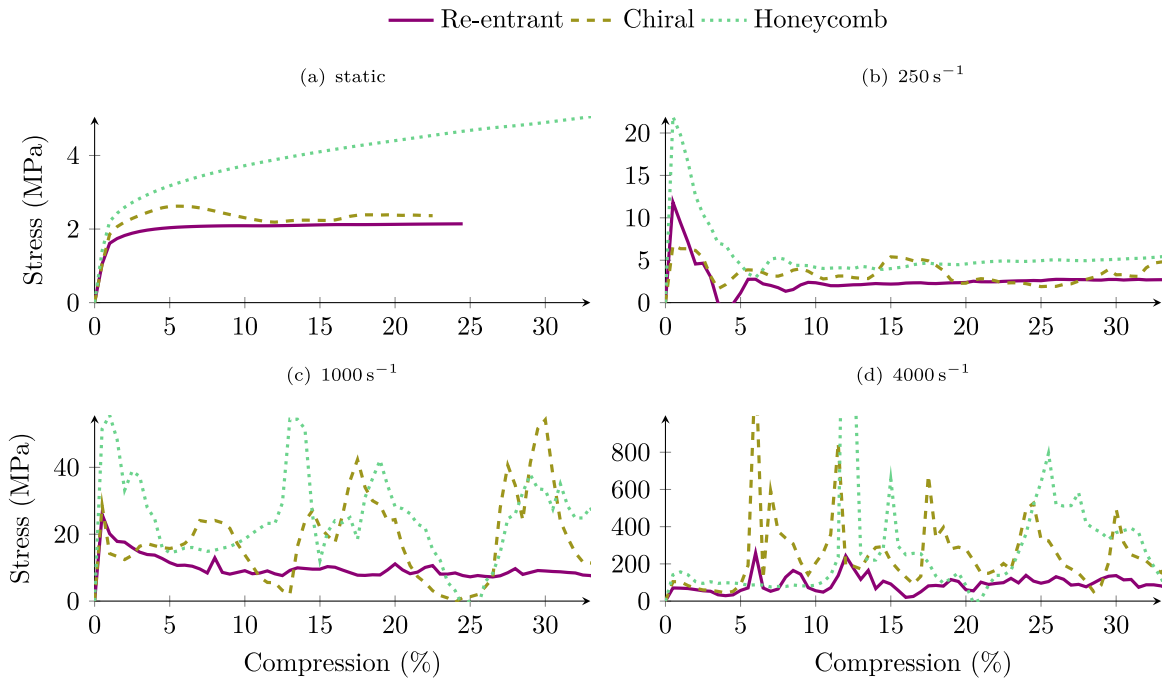

Fig. 4.13. Comparison of the stress–strain curves at the strike face for 8×8 patches of different architectures for the four investigated strain rates.

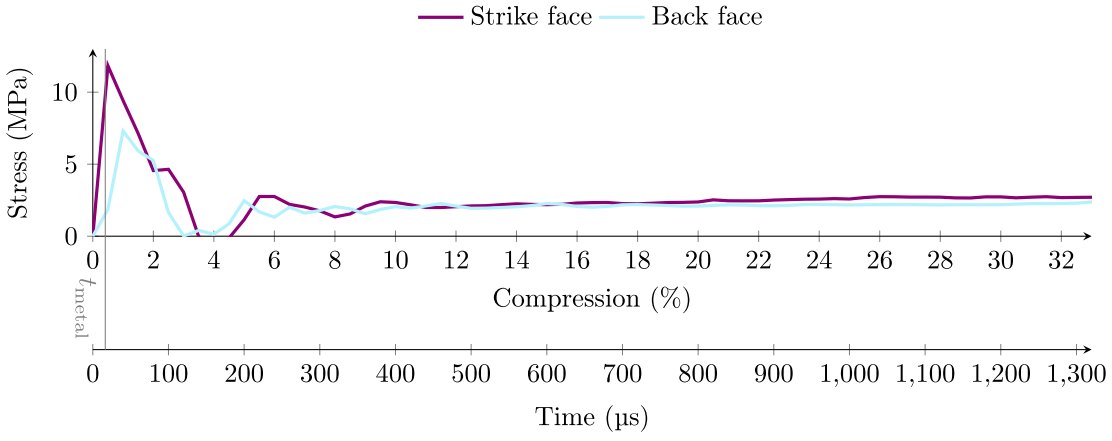

Fig. 5.1. Comparison of the stress on the strike face and the back face under *slow* compression for an 8×8 re-entrant patch.

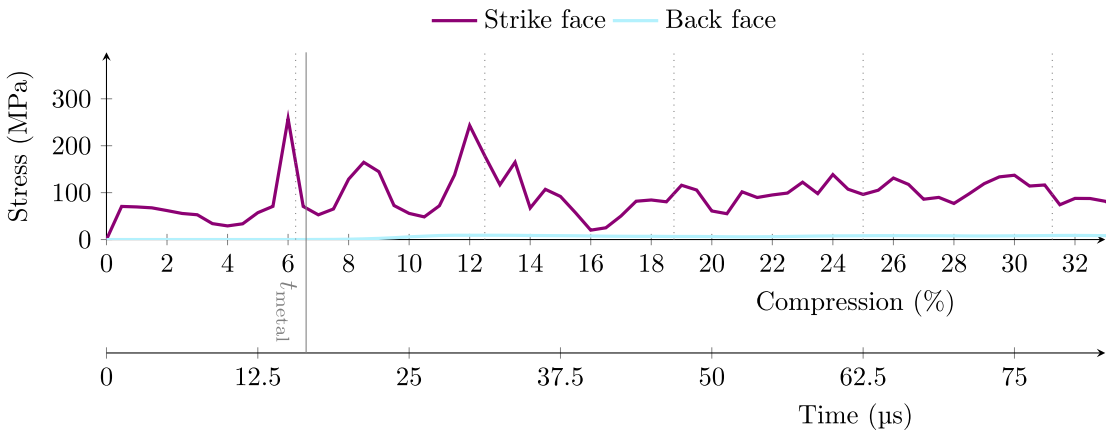

Fig. 5.2. Comparison of the stress on the strike face and the back face under *fast* compression for an 8×8 re-entrant patch.

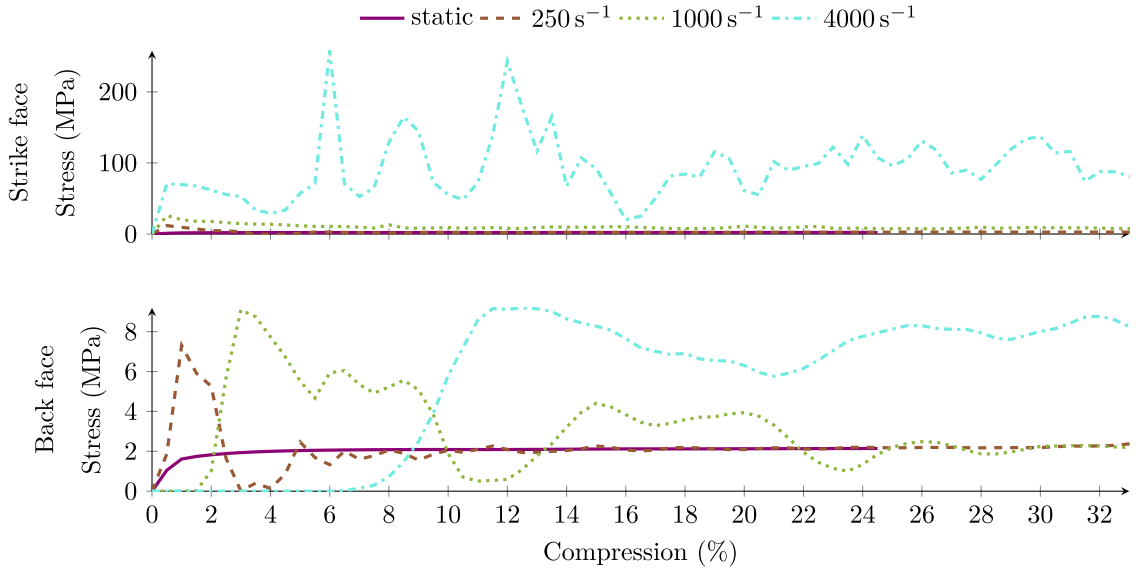

Fig. 5.3. Stresses on both faces for the re-entrant patch for different compression rates.

increase seen here between the different compression rates is however small, when compared to the increase in stresses on the strike face, leading to the assumption, that the stress transmitted to the back face, after an initial peak, is in a first approximation independent of the compression rate. These initial peaks show similar magnitudes irrespective of the compression rate. The stresses transmitted to the back face are reduced when compared to the stress experienced at the strike face. This is mostly due to an increase in the dynamic stresses at the strike face, whilst the stresses at the back face have about the same magnitude. The mechanisms of dissipation of these forces will be discussed in Section 6. Plots comparing the stresses at the strike face and the back face for *static* and *medium* rate compression can be found in Appendix B.1.

5.2. Chiral patch

Next to the re-entrant architecture also the dynamic effects in the chiral architecture are investigated. The stresses on both faces for *slow* compression are shown in Fig. 5.4. In this figure, the stresses are plotted over both the compressive strain, and the corresponding time. As for the re-entrant case, the theoretical time needed for a pressure wave travelling through a beam $t_{\text{metal}} \approx 28.9\,\mu\text{s}$ is indicated by a vertical line. This time is different from the re-entrant patch due to a different geometry (more explanation given in Appendix B.2). It can be seen in Fig. 5.4, that the pressure wave reaches the bottom significantly later than would be expected by a wave travelling unhindered through a metal beam. This is attributed to the impedance jumps at the sharp kinks in the chiral unit cell, leading to partial reflection and conversion from pressure to shear waves. Similar to the re-entrant patch, also for the chiral patch, the stress on both faces converge towards the same value. This convergence is slower than for the re-entrant patch, which is consistent with the longer times required for the stress waves to transverse the patch.

In Fig. 5.5 the stresses for *fast* compression of the chiral patch are depicted. The peaks can again be attributed to the acceleration of horizontal rows of beams at half unit cells. A delay of the pressure waves reaching the bottom of the patch, as discussed above for *slow* compression, can be seen again for the *fast* compression case. The point where the stress on the back face starts to be observable is well beyond the plotted range of 82.5 µs. Prior to this, stress on the back face is insignificant at well below 1 MPa.

In order to get a better estimation of the effect different strain rates have on the response of the chiral patch, the stresses on both faces for different strain rates are compared in Fig. 5.6. As is the case for the re-entrant patch, the chiral patches show an increase of stress needed for the compression of the patch at the strike face with an increase in rate. This increase is moderate for *slow* and *medium* rate compression, and again significantly more pronounced for the *fast* rate. The stresses

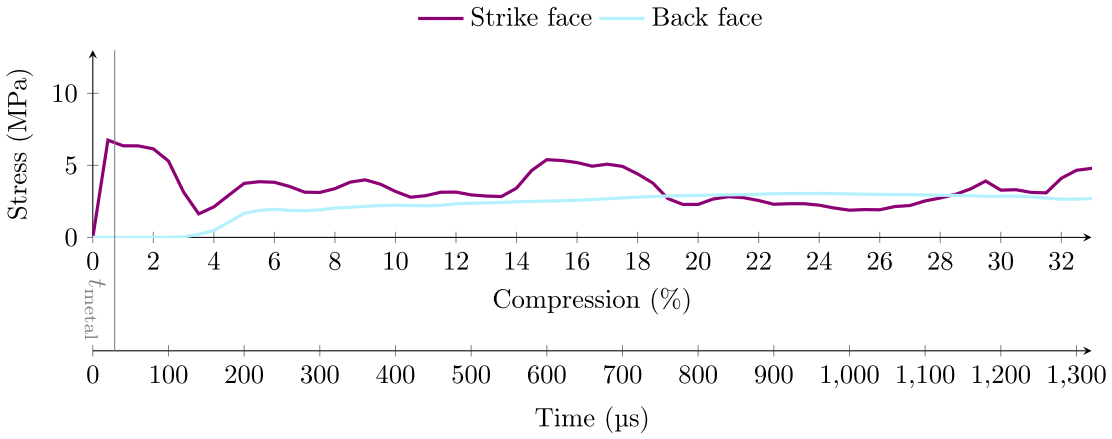

Fig. 5.4. Comparison of the stress on the strike face and the back face under *slow* compression for an 8×8 chiral patch.

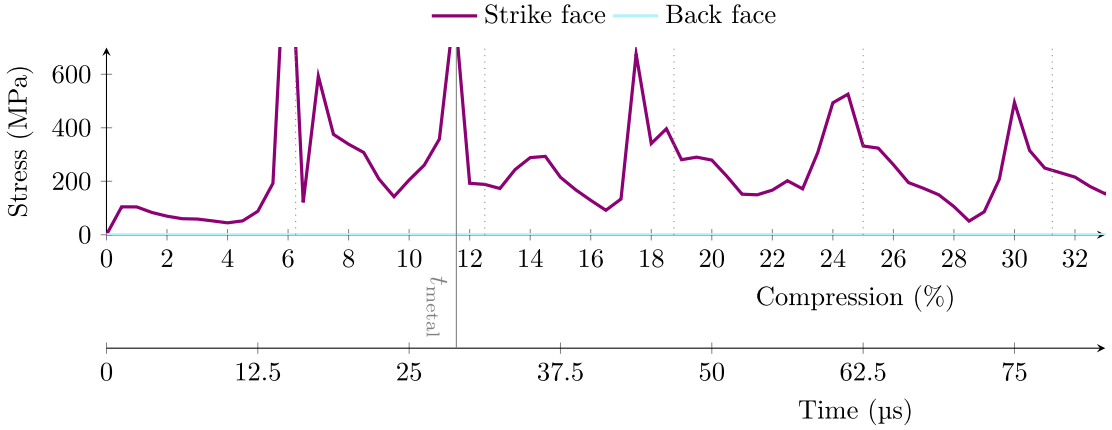

Fig. 5.5. Comparison of the stress on the strike face and the back face under *fast* compression for an 8×8 chiral patch (the values of the peaks outside the figure axis are approximately 1250 MPa at 6 % compression and approximately 800 MPa at 11.5 % compression).

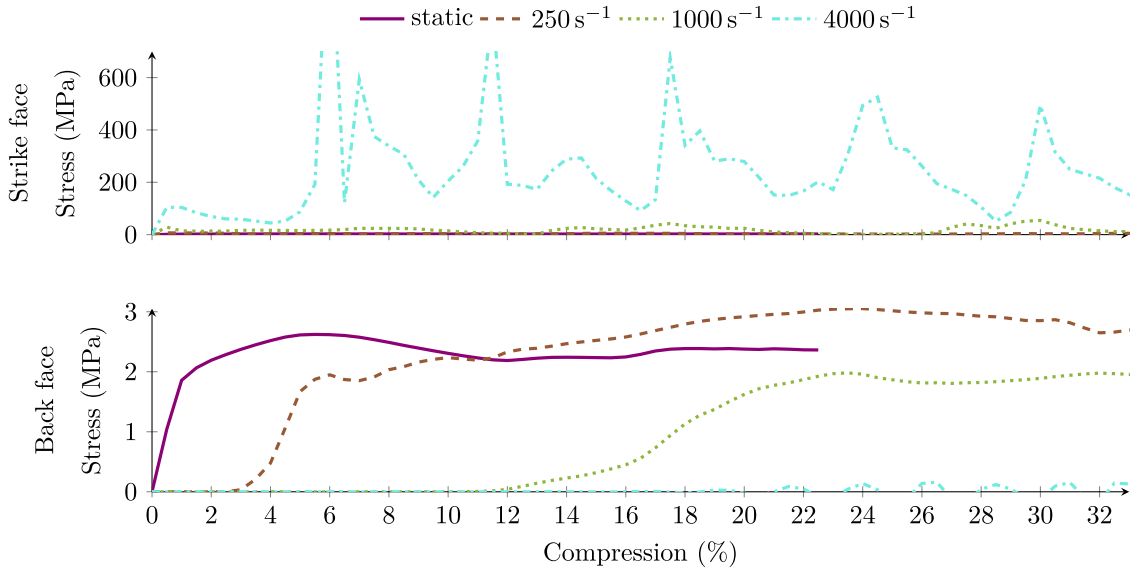

Fig. 5.6. Stresses on both faces for the chiral patch for different compression rates.

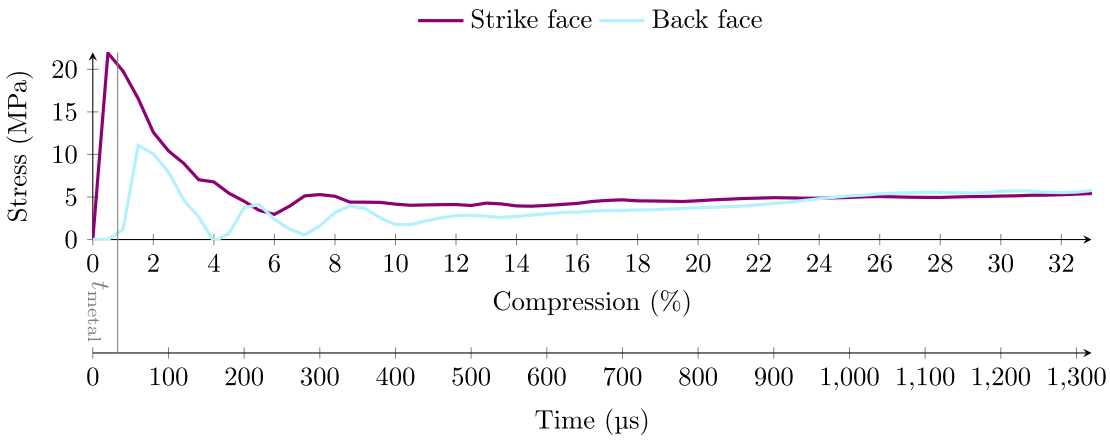

Fig. 5.7. Comparison of the stress on the strike face and the back face under *slow* compression for an 8×8 honeycomb patch.

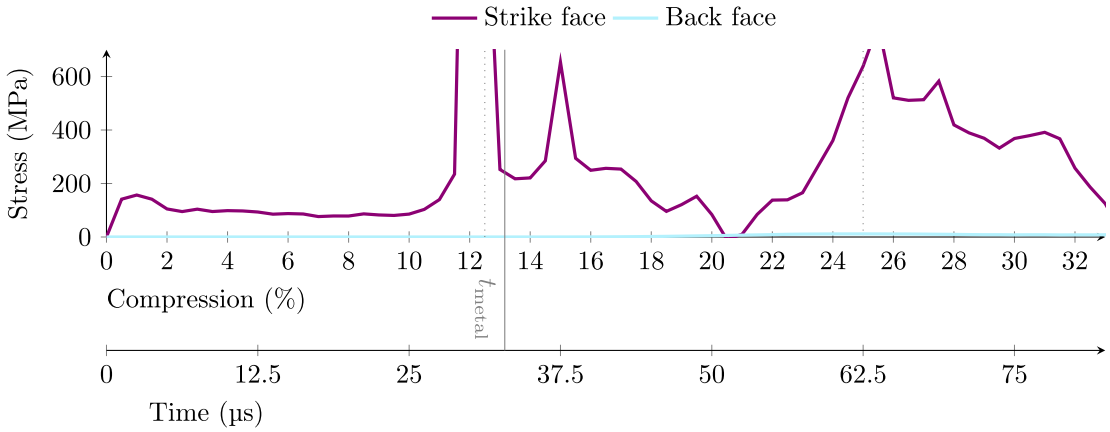

Fig. 5.8. Comparison of the stress on the strike face and the back face under *fast* compression for an 8×8 honeycomb patch (the values of the peaks outside the figure axis are approximately 2500 MPa at 12 % compression and approximately 900 MPa at 25 % compression).

on the back face are less evidently approaching a common value as is the case for the re-entrant patch. Although the compression at *static*, *slow*, and *medium* rates seem to converge towards the same value, a longer time interval is needed in order to assess this effect in more detail. This longer time interval is also needed to be able to give an indication on the effects of the *fast* compression onto the stresses seen at the back face, as the pressure waves through the material need more time to reach the back face of the patch. This longer time interval relates to higher compression, which results in densification and thus a response more akin to a solid material and no longer a heterogeneous metamaterial. At this stage of densification, the formulation of the contact stiffness reaches a limit as well, and a more sophisticated modelling of the contact would be required. It is thus opted not to conduct these simulations. Plots comparing the stresses at the strike face and the back face for *static* and *medium* rate compression can be found in Appendix B.2.

5.3. Honeycomb patch

The behaviour of non-auxetic honeycombs under dynamic compression is investigated as well. The stresses on the strike face and back face for the honeycomb patches, at *slow* rate compression, can be seen in Fig. 5.7. The time for the pressure wave to propagate through the metal $t_{\text{metal}} \approx 32.9\,\mu\text{s}$ is indicated by a vertical line (see Appendix B.3). The general behaviour of the honeycomb unit cell patch, does not deviate from the auxetic unit cell patches. The time delay for the stresses at the back face to rise roughly corresponds with the metal wave speed. Later on stresses on both the front and strike face converge towards a common plateau.

The behaviour of the honeycomb patch for the *fast* rate compression, as seen in Fig. 5.8, shows again lower stresses on the back face compared to the stresses on the strike face. Whilst the forces seen on the back face have a similar order of magnitude compared to the re-entrant unit cells (5 MPa), the stresses on the strike face appear higher at orders of magnitude of 200 MPa. This is consistent with the observations for the auxetic patches.

For a better understanding of the strain rate effect in the non-auxetic patch, the stresses on both faces are shown for the different investigated strain rates in Fig. 5.9. As with the auxetic patches, we can see the stress on the back face for *slow* compression approaching the stress level for the *static* compression. The stress for *medium* compression shows large oscillations around the same level as well. Finally, at *fast* compression, the stress appears to be higher, which is in agreement with the observations made for the auxetic unit cells. This increase is however negligible when compared to the increase in stress at the strike face. A much higher increase in stress on the strike face is needed to compress the patch at the *fast* rate compared to the *medium*, *slow*, and *static* compression cases, which is seen in the auxetic patches as well. Plots comparing the stresses at the strike face and the back face for *static* and *medium* rate compression can be found in Appendix B.3.

5.4. Comparison of patches

Summarizing the findings of this section, two observations can be made: Firstly, that the speed of the pressure waves through the metal

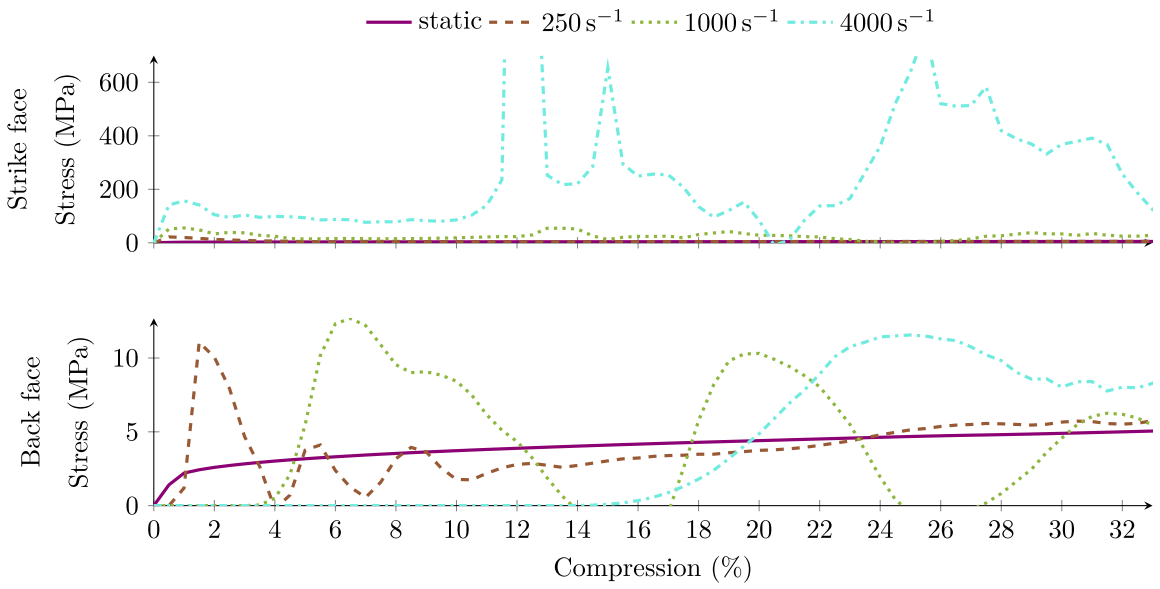

Fig. 5.9. Stresses on both faces for the honeycomb patch for different compression rates.

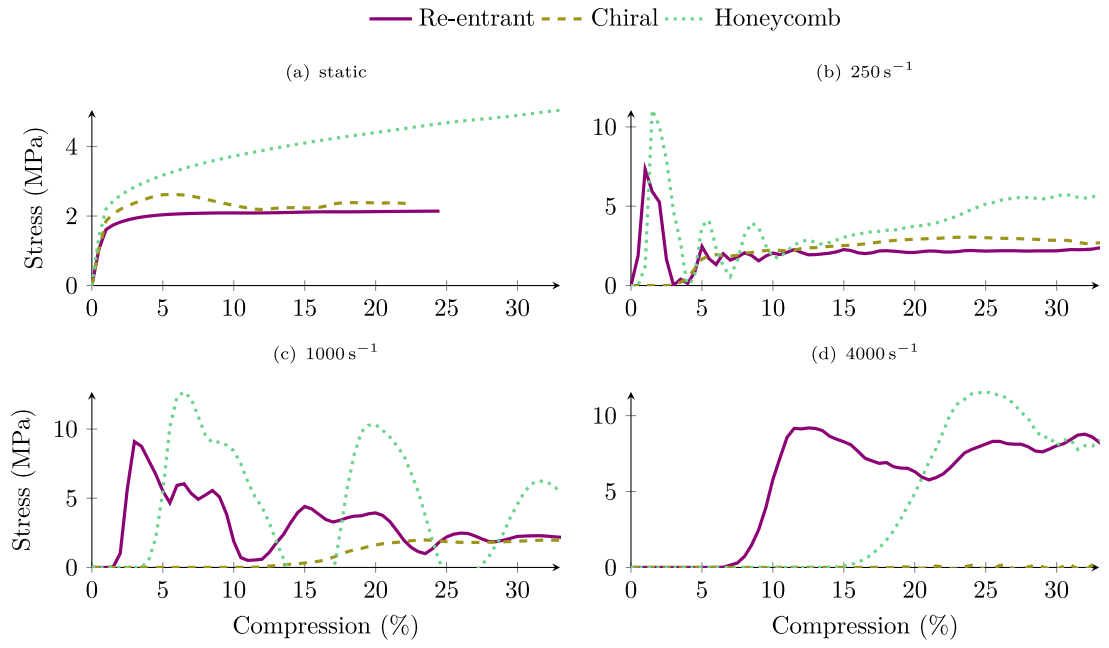

Fig. 5.10. Comparison of the stresses at the back face for 8×8 patches of different architectures for the four investigated strain rates.

is a lower bound for the stress to reach the back face. This theoretical phenomenon can also be observed in the simulations. This lower bound is approached when more straight beams and fewer kinks and joints are present within an architecture, resulting the chiral patch in a significant delay after the theoretical lower limit. Secondly, the stress amplitudes experienced at the back face appear to be largely unaffected by the strain rate, which again is consistent with the results from literature for smaller ranges of strain rates ($\sim 15\,\mathrm{s}^{-1}$ to $625\,\mathrm{s}^{-1}$) at the strike face [22]. The peak stresses experienced in all investigated rates can be regarded as equivalent, and the final, constant stress level approaches the static compression value for all investigated structures. However, this is only a first approximation; a full understanding of the impact protection effect of the different patches requires the consideration of the force-time record and subsequent effects on the protected material.

Both observations can also be seen by comparing the stress curves at the back face of the three patches in Fig. 5.10. In this figure, the first effect is clearly observable as the rise in stress level appears later for patches with less straight connections between the top and the bottom. For instance, both the re-entrant and the honeycomb unit cell can be considered. The beams of the re-entrant patch are 24.4° off the vertical, whereas the beams for the honeycomb patch are 29.7° off, meaning the re-entrant patch offers a more straight vertical line for the pressure waves to the bottom compared to the honeycomb patch. The angle is however not the only factor for the time of the waves reaching the back face, as can be seen by the much later rise in stress for the chiral patch, of which the beams are only 28.1° off the vertical, but exhibit more kinks and joints when compared to the other two architectures. The chiral architecture contains beams meeting in 90° angles at their joints, amplifying this effect. Comparing the stress levels at the back face between the architectures, *static* compression shows the same graph as the strike face, resulting in Fig. 5.10a being identical to Fig. 4.13a. Considering higher compression rates, the chiral

architecture appears to show the lowest stress levels at the back face, despite showing similarly high stress levels at the strike face compared to the honeycomb structure. This observation is based on the *slow* and *medium* compression rates, as in the *fast* compression rate, the stress does not reach the back face for the chiral patch within the investigated time, however a qualitatively similar result is to be expected. The fact, that the stress waves reaching the back face are significantly smaller than the stresses seen at the strike face also indicates that the fixed boundary conditions do not introduce spurious effects by reflection of stress waves and subsequent interference

All the results presented in this section indicate the chiral architecture as a good candidate for impact mitigation.

6. Local energy distributions

In order to facilitate a more thorough understanding of the mechanisms exhibited in the previous section, the SEA, as defined by Eq. (8) spent on compression of the patches and its subsequent distribution into various components of energy throughout the patches is analysed. For the present analyses, the global specific energy is split into elastic potential energy, inelastic dissipated energy, and kinetic energy. The spatial distribution of the elastic, dissipated, and kinetic energy measures over the two directions of the patch, based on the nodal energy levels as explained in Section 3, will be analysed as well.

6.1. Re-entrant patch

The first comparison is the distribution of energy in the patch at different compression rates shown in Fig. 6.1 for the re-entrant patch. In Fig. 6.1a, *static* deformation is shown. At around 1 %, plastic deformation starts to occur, which coincides with the loss in stiffness seen in Fig. 4.1. During the remainder of the analysis, the approximately 85 % of the SEA put into the system is dissipated through plastic deformation, and only about 15 % is seen in potential energy. In Fig. 6.1b, the distribution of energy for *slow* compression is shown. At later stages of the deformation, the share of dissipated energy remains roughly the same at about 85 % and the potential energy (at about 7 %) is already surpassed by the kinetic energy at about 8 % of the total SEA spent on compressing the material. In Fig. 6.1c, the distribution of energy in the *medium* compression scenario is shown. While the dissipated energy is still the dominant form of energy present in the system with taking up about two thirds, the amount of kinetic energy increases to nearly one third of the SEA whilst the potential energy vanishes to less than 3 % during the deformation. This effect is visible in a more pronounced way in Fig. 6.1d, showing both contributions of the kinetic and dissipated energy taking up nearly half of the energy share each. Note, that the force peaks observed in Fig. 5.2, can be seen in the energy plots as well. At the half unit cell points — at multiples of 6.25 % — the kinetic energy shows a sharp increase.

Next to the distribution of energy for different physical mechanisms, the distribution of energy across the lattice structure is investigated. In Fig. 6.2, the deformation after 20 % *static* compression is depicted with marginal distributions of the energy density split into the different physical mechanisms shown at the top and the right of the patch. While the symmetry between the left and the right side remains intact, the top-bottom symmetry is broken by the more localized deformation near the bottom. The plastic nature of this collapse is emphasized by a higher specific dissipated energy near the bottom of the patch.

In Fig. 6.3 the vertical distribution of the absorbed energy is shown for the four investigated rates. Comparing the *static* results to the *slow* rate compression case, in Figs. 6.3a and 6.3b respectively, confirms the observation from Fig. 6.1, that the dissipated energy is responsible for the majority of the SEA needed to compress the patch. Only a minor portion of the SEA is stored in potential energy, and at *slow* compression, the kinetic energy contributions are of course comparatively small. A shift of the energy distributions towards the strike face at the top of the patch is however observed. This shift in the distributions can be seen more pronounced in Fig. 6.3c for the *medium* rate, where the dissipated energy still takes up the majority of SEA, as discussed above. At *medium* compression, although more than 80 % of the energy are at the top eighth, still about 10 % are in the second eighth and about 10 % in lower parts of the structure. This is no longer the case for the *fast* compression rate seen in Fig. 6.3d, where more than 99.5 % of the total energy are in the top eighth of the structure. For this rate, the amounts of energy seen at the lower parts of the structure appear negligible, and the energy distributions show a clear increase in the relative share of kinetic energy, which is in agreement with the observations from Fig. 6.1. This negligible amount of energy in the lower parts of the structure is in agreement with the deformation patterns shown in Fig. 4.4. As discussed above, the deformations remain small in the lower parts of the patch at this *fast* rate, as also can be seen by the lack of lateral contraction at the boundaries, that would be expected from the negative Poisson's ratio of this structure, resulting in negligible amounts of energy in the lower parts of the patch.

6.2. Chiral patch

The energy distribution in the chiral patch under different deformation rate is analysed in the same manner. In Fig. 6.4, the distribution of the SEA in potential, kinetic, and dissipated energy is shown for different rates. The observations made for the re-entrant patch hold for the chiral patch as well. At *static* deformation, the majority of the SEA spent on compressing the material is dissipated throughout the deformation and only a minor increase in potential energy due to hardening of the material can be seen. At higher strain rates, the total SEA increased, as well as the share of kinetic energy. The share of kinetic energy at the *medium* rate is already half of the total energy, whereas for the re-entrant patch, this only happens at the *fast* rate, indicating an increased rate sensitivity of the chiral lattice. This increased strain-rate sensitivity is consistent with the softening response seen in the static considerations in Fig. 4.5, where the chiral architecture shows a softening response amplifying the localization of deformation. The localization of deformation due to dynamic effects interacts with the localization of deformation due to static instabilities leading to a stronger reaction to dynamic compression, that is already visible at lower compression rates. The higher sum of the different forms of specific internal energy compared to the externally computed SEA seen in Figs. 6.4b and 6.4d is due to interpenetration of singular beams, that lead to divergence in the *static* case (Fig. 4.5) and represent an unphysical source of energy in the dynamic simulations. Since this effect is small (less than 8 % in all simulations conducted) and does not influence the global behaviour of the lattice, it is deemed acceptable.

The strain rate sensitivity of the chiral patch, can also be seen when comparing the vertical distributions of energy in Fig. 6.5. In this figure, the vertical distribution of energy throughout the patch is plotted for the four investigated rates. In Figs. 6.4c and 6.4d, depicting the *medium* and *fast* rate compression, the complete concentration of energy at the top is shown. This is consistent with the observations made in Fig. 6.4 and further emphasizes the increased strain rate sensitivity of the chiral architecture when compared to the re-entrant architecture. The increased strain rate sensitivity can be observed as well when investigating the fraction of energy in the top eighth of the patch. At *medium* rate is it already over 97.5 % and reaches over 99.99 % at the *fast* rate. The chiral patch at *low* rate compression, shows a similar trend compared to the re-entrant patch. A small shift of energy towards the top can be observed, with the energy in lower parts being more uniformly distributed. A similar shift of energy towards the top can be observed in *static* compression in Fig. 6.5a, this is however explained by the localized deformation in singular rows of unit cells, as shown in Fig. 4.6, where the deformation corresponding to this distribution is shown for the 8×8 patch at 20 % compression. The localization of deformation around the unit cells corresponds with a significant increase in energy dissipated and only a minor increase in elastically stored energy, as shown in Fig. 6.5a.

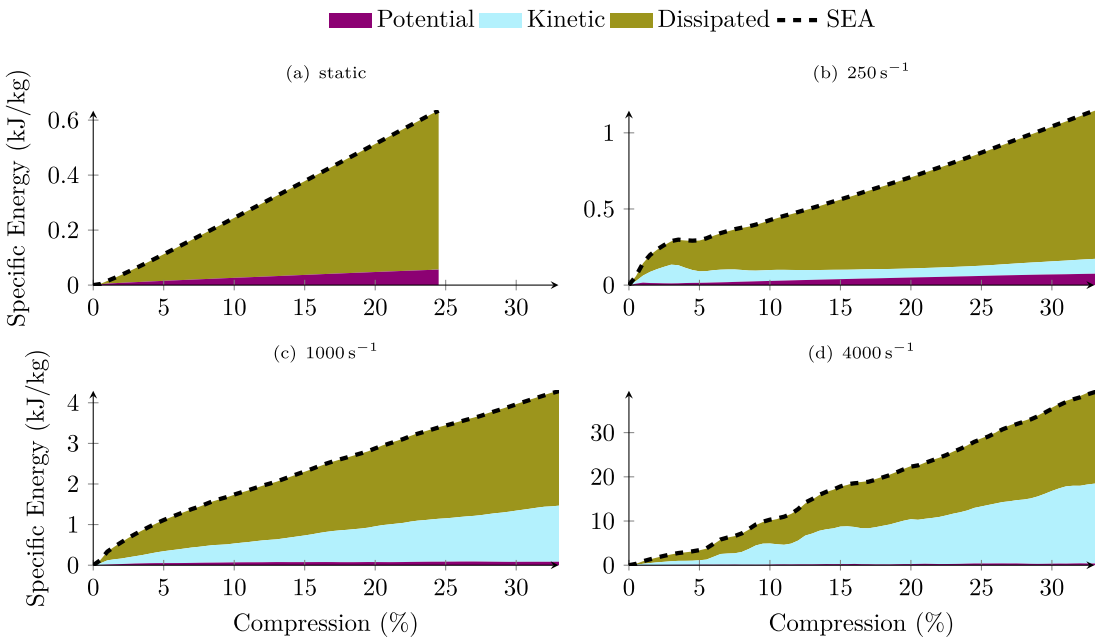

Fig. 6.1. Distribution of the SEA into different types of energy for the 8×8 re-entrant patches at different strain rates.

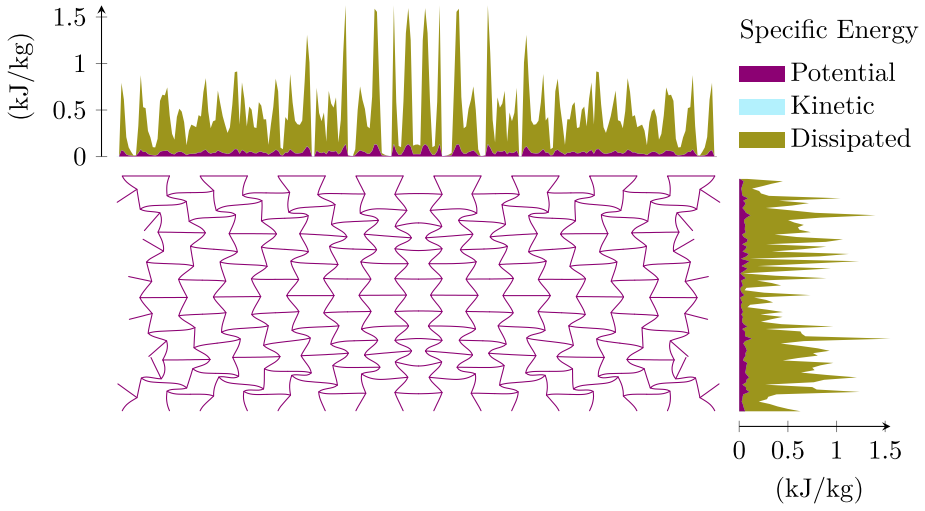

Fig. 6.2. Local distribution of energy at 20 % compression for *static* compression of the 8×8 re-entrant patch.

6.3. Honeycomb patch

Finally, the distribution of energy in the honeycomb patch is investigated. In Fig. 6.6, the different forms of energy are again compared for *static*, *slow*, *medium* and *fast* rates of compression. Here, the phenomena observed in the re-entrant and chiral patch, can be seen as well. The majority of the energy is dissipated and the fraction of kinetic energy rises with increasing compression rate. Two observations are noteworthy: Firstly, the peaks in force on the strike face observed at *fast* compression, seen in Fig. 5.8, correspond with the sudden rise of kinetic energy in Fig. 6.6d as well. In Fig. 4.12 the acceleration of horizontal bars is illustrated, leading to both force peaks and a fast rise in kinetic energy. Secondly, at *medium* rate compression, the kinetic energy takes less than half of the energy in the patch, resembling the behaviour of the re-entrant patch, distinct from the chiral patch. This is seen by the vertical distributions of energy in Fig. 6.7 as well. Here, at *medium* rate, the energies are shifted to the upper boundary, but still a significant amount of energy is in the bottom part of the lattice, similar to the observations made for the re-entrant patch. This is no longer the case for the *fast* rate, where energy is to approximately 95 % concentrated in the upper eighth next to the strike face. At *slow* compression, a nearly linear distribution of all energies rising from the bottom to the top can be seen, with more energy dissipated close to the strike face. *Static* compression shows a bulge in the centre of the patch, consistent with the global barrelling seen in Fig. 4.10. The peaks near the top and the bottom of the distribution are attributed to the strong deformation of elements at the fixed boundaries.

6.4. Comparison of patches

There are two commonalities between different metamaterial architectures when considering the energy distributions. Firstly, the majority of energy spent on compressing the material is dissipated by plastic deformation of the material throughout all compression rates. At higher rates the amount of kinetic energy approaches the level of plastically dissipated energy in the patch. This corresponds to the second common effect at higher rates, noted in earlier sections. The behaviour is not

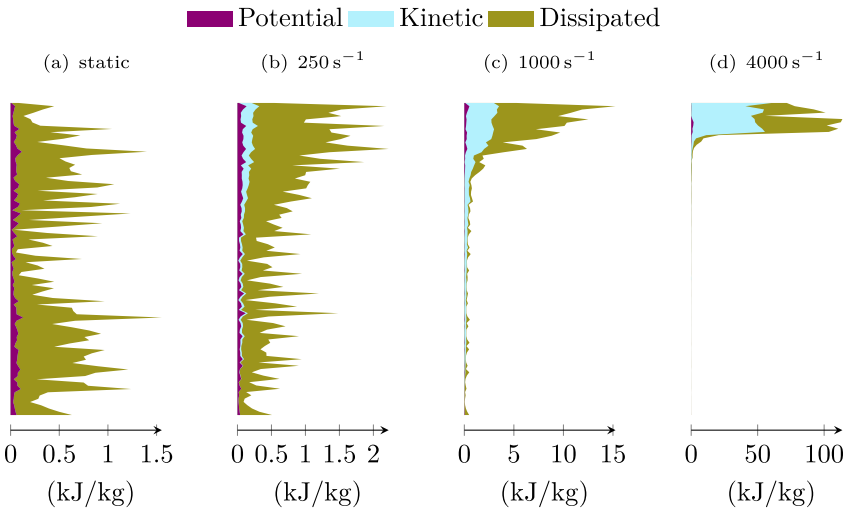

Fig. 6.3. Vertical distribution of energy at 20 % compression for all investigated compression rates in the 8×8 re-entrant patch.

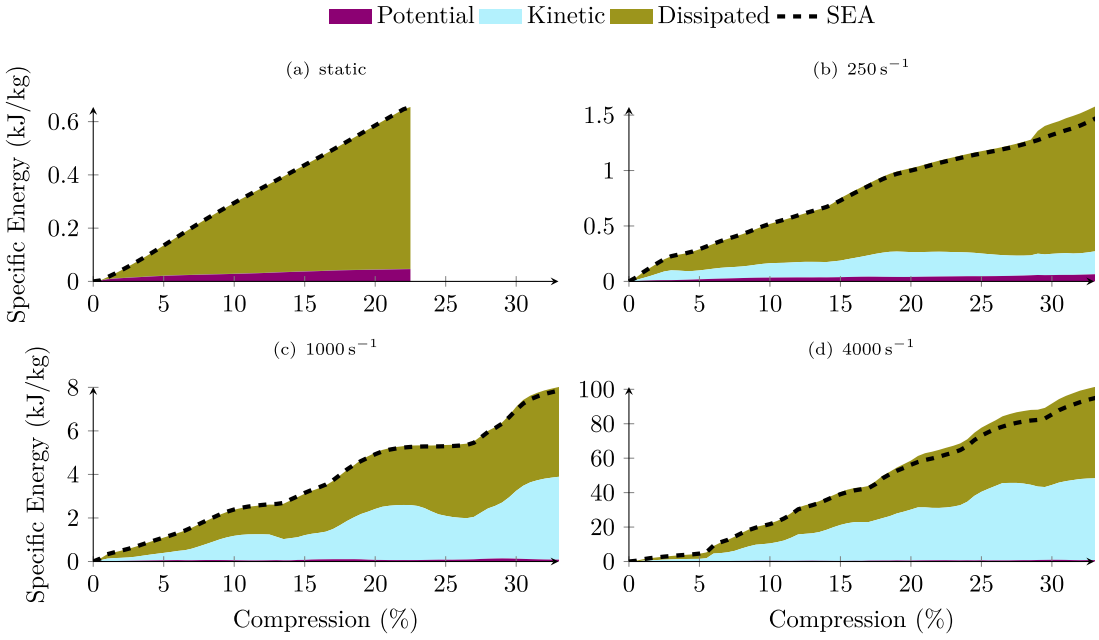

Fig. 6.4. Distribution of the SEA into different types of energy for the 8×8 chiral patches at different strain rates.

determined by the transmission of forces, but rather by the inertial forces that result from the distribution of mass within the lattice.

For a fair comparison of the different architectures, the SEA is plotted against the compression for the three investigated architectures. In Fig. 6.8a, the SEA can be seen for *static* compression. Here, the honeycomb architecture shows the highest levels, which is consistent with the higher levels of pressure seen for this architecture in Fig. 4.13. The honeycomb patches show the highest SEA for the investigated strain rates, which is consistent with the reports from literature [22,24]. For *fast* compression, it is noteworthy, that the chiral patch shows similar levels of energy absorption as the honeycomb architecture up to 12 %, at which compression levels the first contact occurs for the honeycomb leading to a steep rise in absorbed energy. This emphasizes the dominance, that inertial effects have over the structural response of the different architectures at high rates of deformation.

7. Conclusion

The investigations presented in this article offer a novel perspective on the high-rate deformation mechanisms in different architected metamaterials employed for impact mitigation.

It has been shown in Section 4, that localized failure within the investigated auxetic architectures — re-entrant and chiral — leads to a stronger softening effect for smaller unit cells due to a more pronounced localization of the deformation. However, honeycombs, as an investigated non-auxetic architecture, show a global deformation

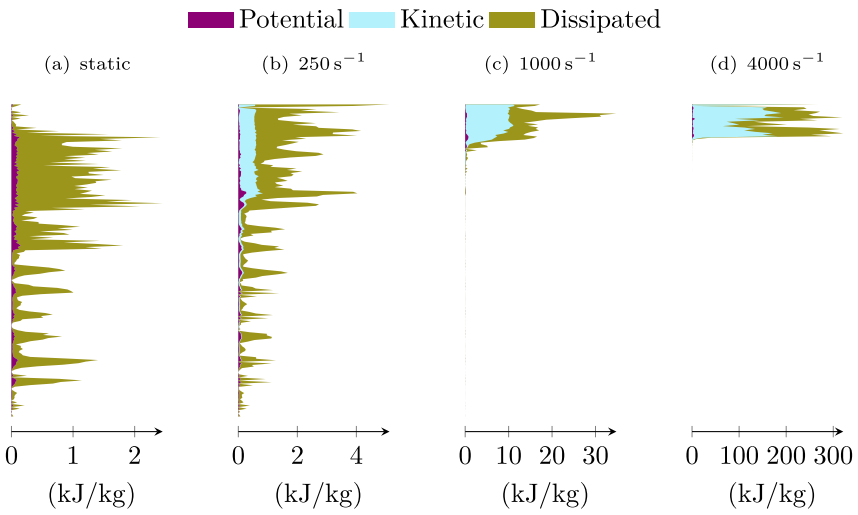

Fig. 6.5. Vertical distribution of energy at 20 % compression for all investigated compression rates in the 8×8 chiral patch.

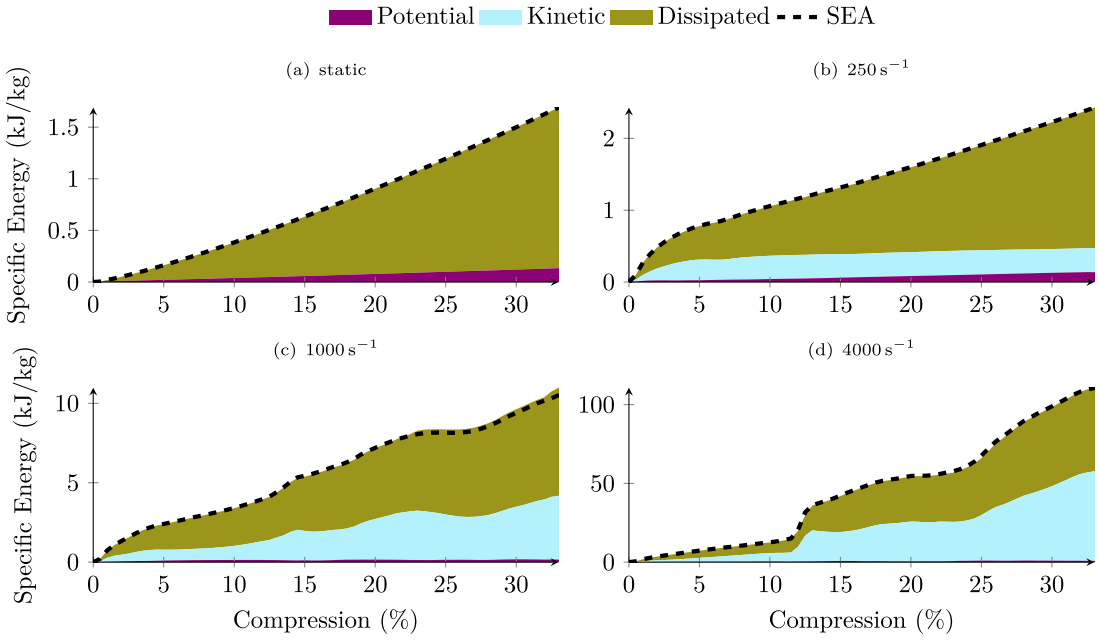

Fig. 6.6. Distribution of the SEA into different types of energy for the 8×8 honeycomb patches at different strain rates.

pattern, leading to a stiffer response when considering patches with more unit cells. For higher rates, there is a shift towards deformation localizing at the strike face, leading to a more brittle response, amplified by the static softening effects, and unit cell size dependence for all architectures. The subsequent deformation resistance is dominated by inertia effects, that are directly related to the geometry of the microstructure of the patch.

Next to the stresses at the strike face, also the stress levels at the back face have been investigated in Section 5. In this investigation it has been shown, that the force exerted on the back face is delayed by the wave transmission through the lattice of the metamaterials. The magnitude of the transmitted forces has been shown to be, in a first approximation, independent of the compression rate. Only at the highest investigated compression rate the forces start to rise. This suggests, that for an initial estimation of the force exerted at the back of the protective structure, a set of two calculations, i.e. a static to estimate the terminal level of stress and a high rate analysis to quantify the dynamic pulses at the rear face, might be sufficient to estimate the force transmitted through an architected metamaterial. It should be noted here, that the numerical model employed does not account for any strain rate dependency in the material behaviour and no direct experimental comparison was available. Therefore, further investigations to find a relation between the strain rate dependent behaviour of the base materials and the transmitted forces through the lattice would be needed to assess the behaviour for base materials with a high strain rate sensitivity.

The distribution of different types of energy throughout the structure of the architected metamaterials has been investigated as well in Section 6. In the static case, the concentration of energy at the moment of localized deformation is observed for the auxetic architectures, whereas for the globally barrelling honeycomb structure, the energy is more evenly distributed. At higher strain rates, the distribution of energy is concentrated at the top of the lattice near the strike face, consistent with the localized deformation patterns seen in Section 5. The chiral architecture shows the highest sensitivity to strain rate, whilst the honeycomb architecture shows the largest amount of SEA across the investigated cases. This is consistent with the softening

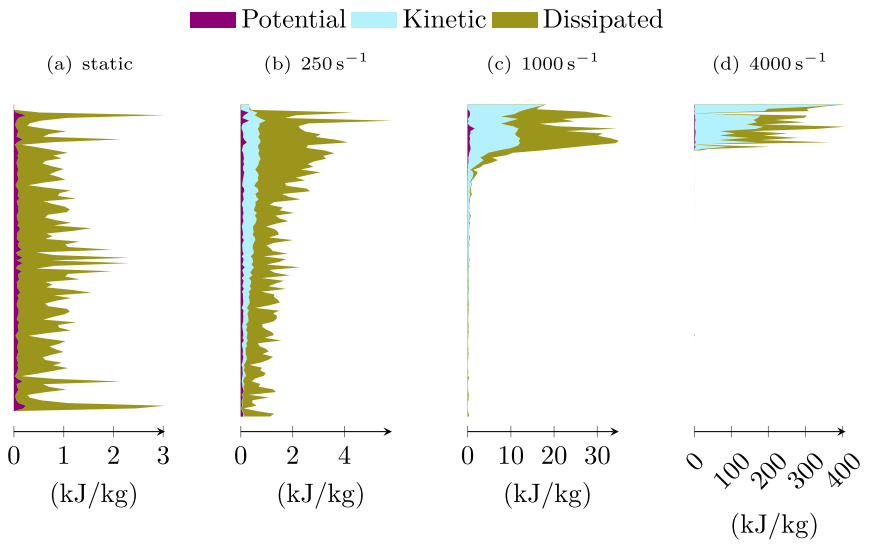

Fig. 6.7. Vertical distribution of energy at 20 % compression for all investigated compression rates in the 8 × 8 honeycomb patch.

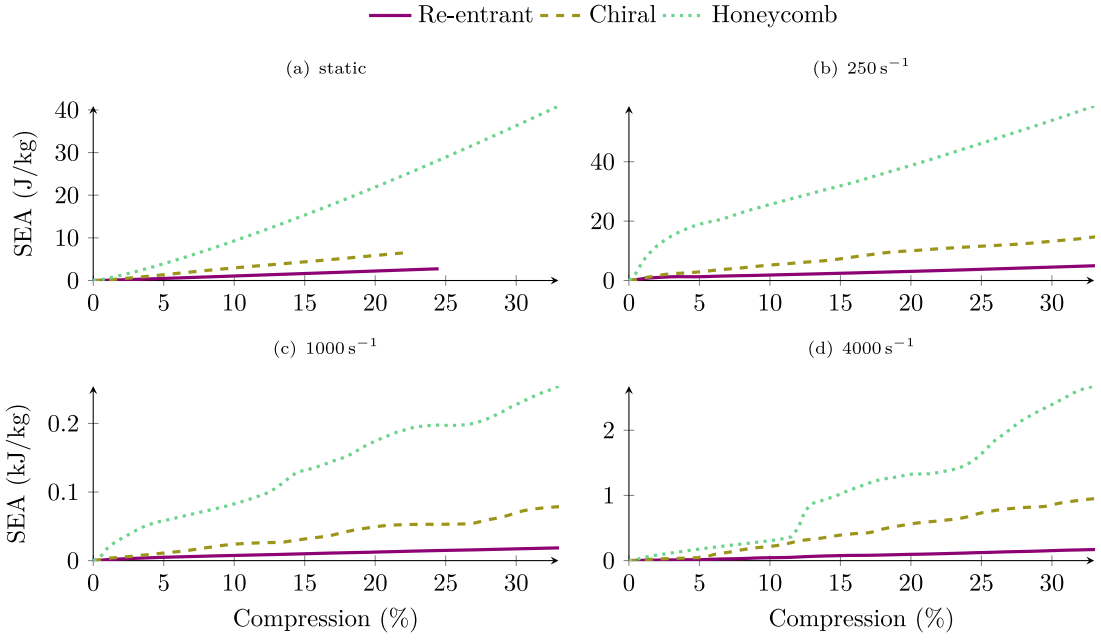

Fig. 6.8. Comparison specific absorbed energies for 8 × 8 patches of different architectures for the four investigated strain rates.

behaviour for the chiral architectures and the hardening behaviour for the honeycomb architectures during static compression.

Throughout this study no beneficial contribution from a negative Poisson's ratio for impact mitigation can be found. As the study is limited to a selected set of architectures and only a single configuration of those is investigated, a more profound study would be needed to generalize this claim. This study showcases the strain rate sensitivity of the investigated architectures relating to both the energy absorbed and the forces transmitted. The evaluation of the forces transmitted is the main difference compared to existing studies in literature (especially [22,24]), where only the forces on the strike face are considered and an advantage for the auxetic structures is assumed based on the lower force levels seen there. Whilst this is the case also when considering the forces on the back face, one should note that both the delay of these forces and the fact, that in our study we assume a constant compression rate, which would not be the case for real world impact. The higher SEA of the honeycomb architecture will lead to lower compression rates later during the impact, leading to lower forces again. Non-auxetic, convex architectures also will densify later, as discussed in literature [22,24], which allows for a longer time for the impactor to be slowed down and the forces to be spread out over a longer time, as shown experimentally [29]. Auxetic structures will lead to a more densified material beneath the impactor at the cost of higher, whether this is desirable needs to be answered considering the threat, that needs to be stopped. The obtained results allow designers of protection concepts to make an informed decision on the architecture and the size of the unit cells based on force transmission during static compression together with an estimation of the maximum force pulse during higher rate compression. Next to the practical applications, also new research avenues have been opened into impact resistant metamaterials away from simply auxetic structures towards architectures that focus on the limitation of the transmitted forces. Here especially metamaterials that further separate the strike face from the back face, such as interpenetrating lattices (cf. [48,49]), and metamaterials that circumvent the force peaks at the front by employing an aperiodic structure (cf. [50,51]).

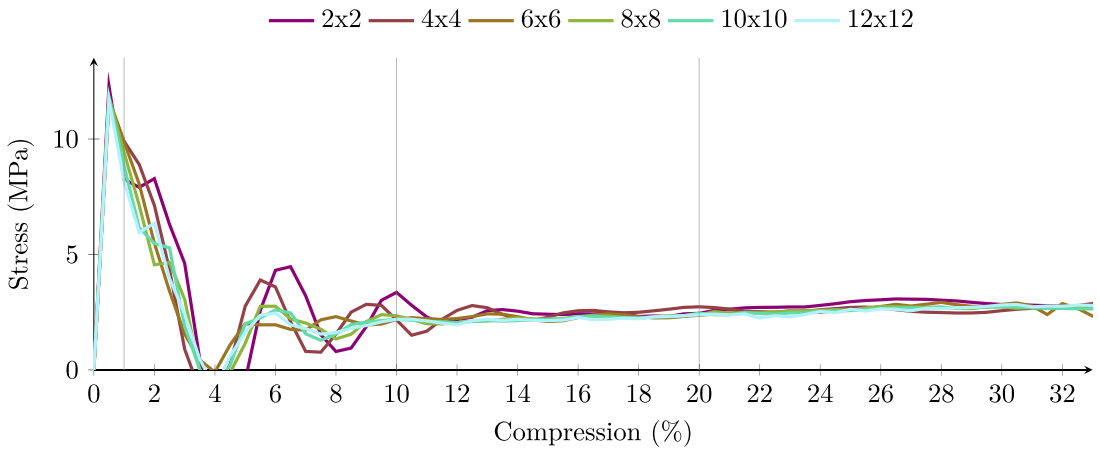

Fig. A.1. Stress–strain curves of patches with a different number of re-entrant unit cells under *slow* rate compression.

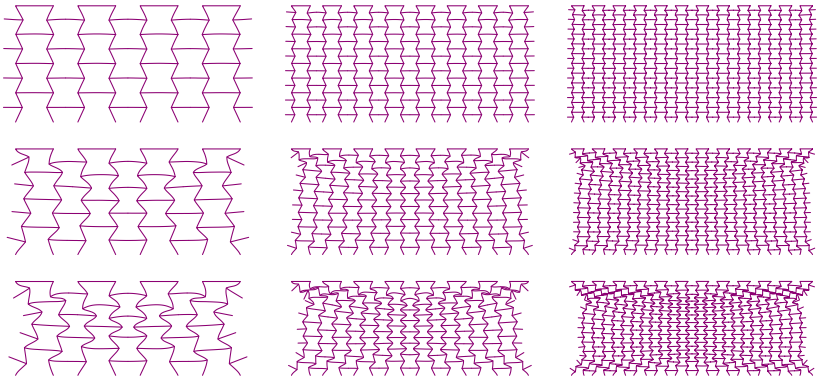

Fig. A.2. Re-entrant 4×4 (left), 8×8 (centre), and 12×12 (right) unit cell patches under *slow* rate deformation at 1 %, 10 % and 20 % compression.

CRediT authorship contribution statement

T. Gärtner: Writing – original draft, Visualization, Validation, Software, Methodology, Investigation, Data curation, Conceptualization. **S.J. van den Boom:** Writing – review & editing, Supervision, Methodology, Conceptualization. **J. Weerheijm:** Writing – review & editing, Funding acquisition, Conceptualization. **L.J. Sluys:** Writing – review & editing, Supervision, Methodology, Funding acquisition, Conceptualization.

Declaration of competing interest

The authors declare that they have no known competing financial interests or personal relationships that could have appeared to influence the work reported in this paper.

Acknowledgements

The project is financed by TNO through the PhD program of the Dutch Ministry of Defence.

The authors acknowledge the use of computational resources of the DelftBlue supercomputer, provided by Delft High Performance Computing Centre (https://www.tudelft.nl/dhpc) [52].

The availability of scientific colour maps [53] used in this publication is highly appreciated.

Appendix A. Additional number of unit cells plots

A.1. Re-entrant unit cells

See Figs. A.1–A.4.

A.2. Chiral unit cells

See Figs. A.5–A.8.

A.3. Honeycomb unit cells

See Figs. A.9–A.12.

Appendix B. Additional strain rate plots

B.1. Re-entrant patch

See Figs. B.1 and B.2.

B.2. Chiral patch

See Figs. B.3 and B.4.

For the chiral patch, the time needed for a pressure stress wave to travel through the metal is computed from the height of the patch $h = 132\,\text{mm}$ and the angle between the beams and the vertical of $\alpha = 28.1°$:

$$t_{\text{metal}} = \frac{h/\cos(\alpha)}{c_{\text{metal}}} \approx 28.9\,\mu\text{s}. \tag{B.1}$$

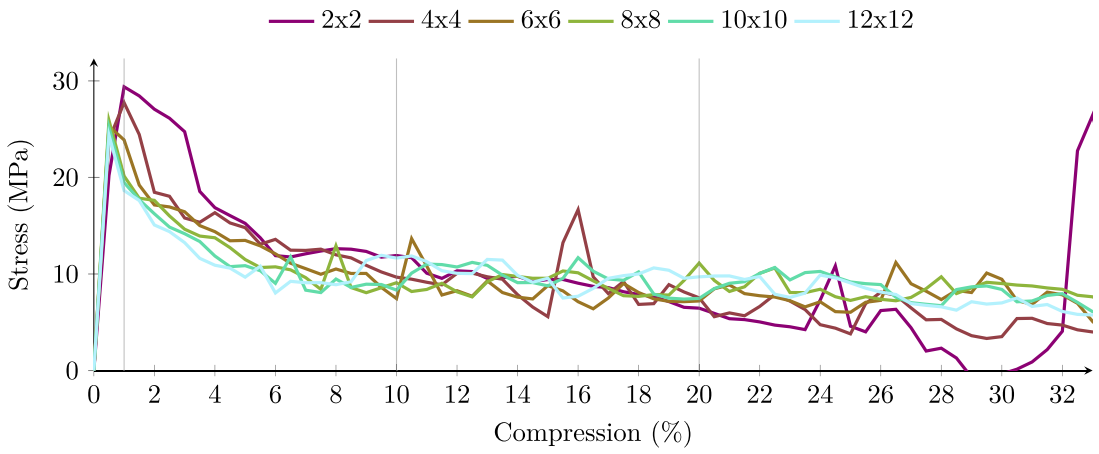

Fig. A.3. Stress–strain curves of patches with a different number of re-entrant unit cells under *medium* rate compression.

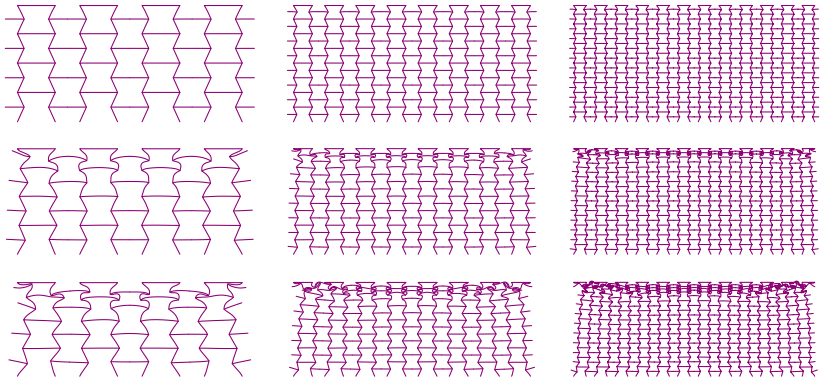

Fig. A.4. Re-entrant 4×4 (left), 8×8 (centre), and 12×12 (right) unit cell patches under *medium* rate deformation at 1 %, 10 % and 20 % compression.

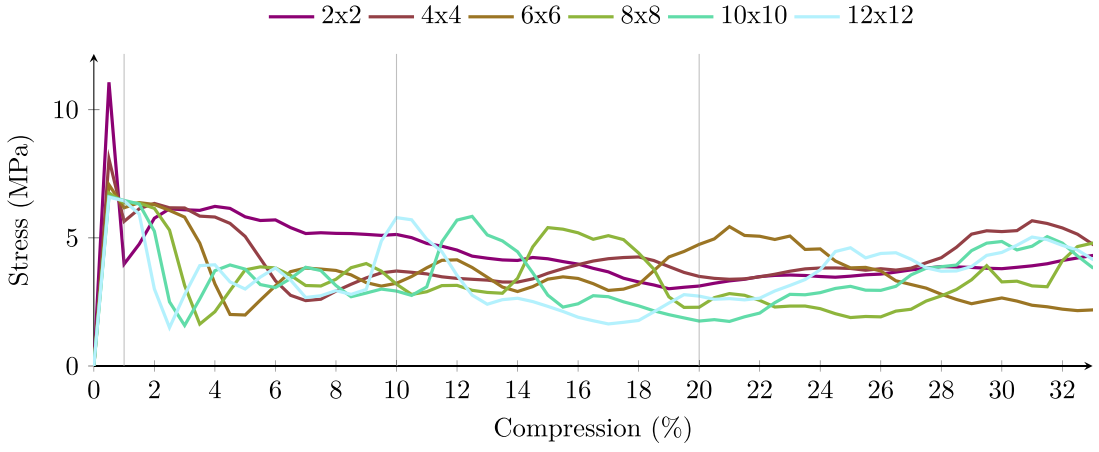

Fig. A.5. Stress–strain curves of patches with a different number of chiral unit cells under *slow* rate compression.

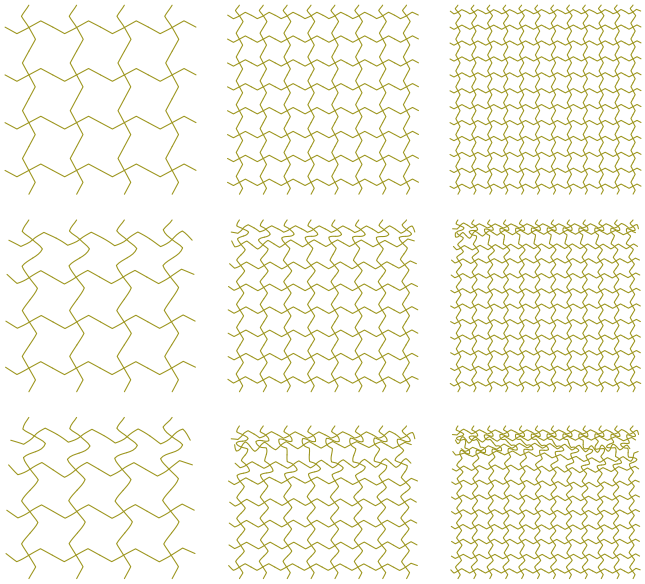

Fig. A.6. Chiral 4×4 (left), 8×8 (centre), and 12×12 (right) unit cell patches under *slow* rate deformation at 1 %, 10 % and 20 % compression.

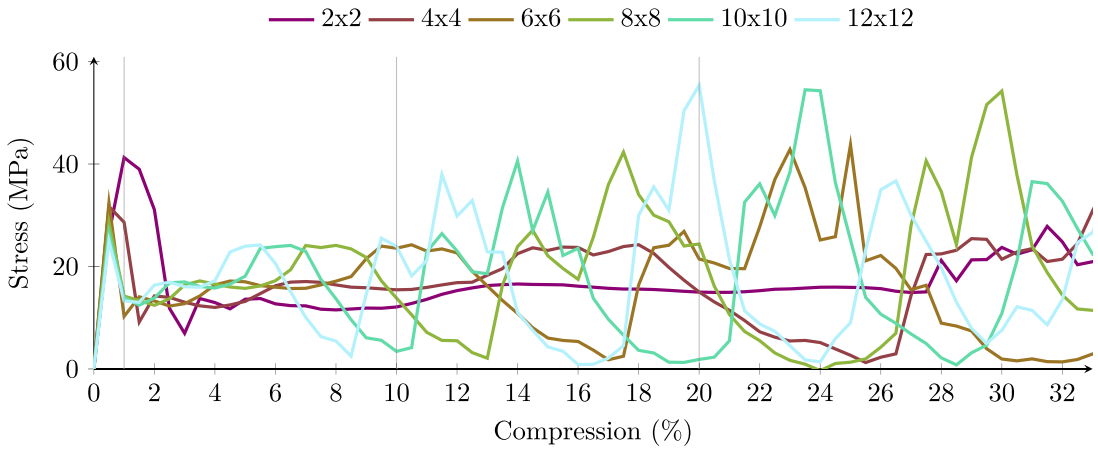

Fig. A.7. Stress–strain curves of patches with a different number of chiral unit cells under *medium* rate compression.

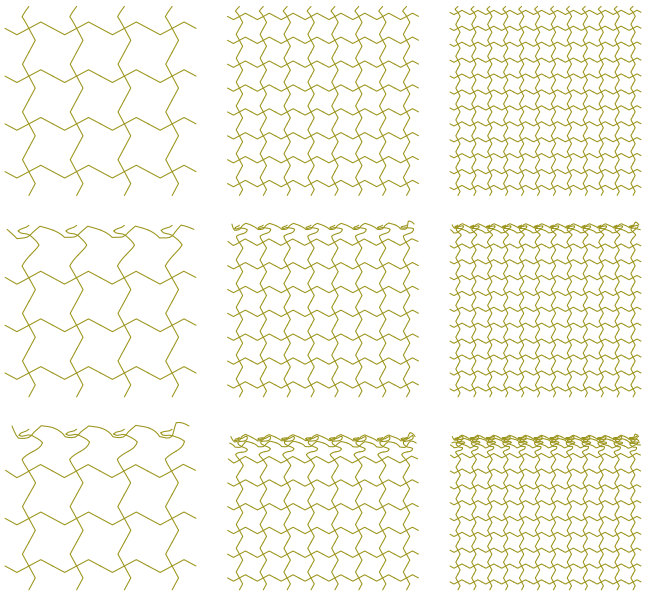

Fig. A.8. Chiral 4×4 (left), 8×8 (centre), and 12×12 (right) unit cell patches under *medium* rate deformation at 1 %, 10 % and 20 % compression.

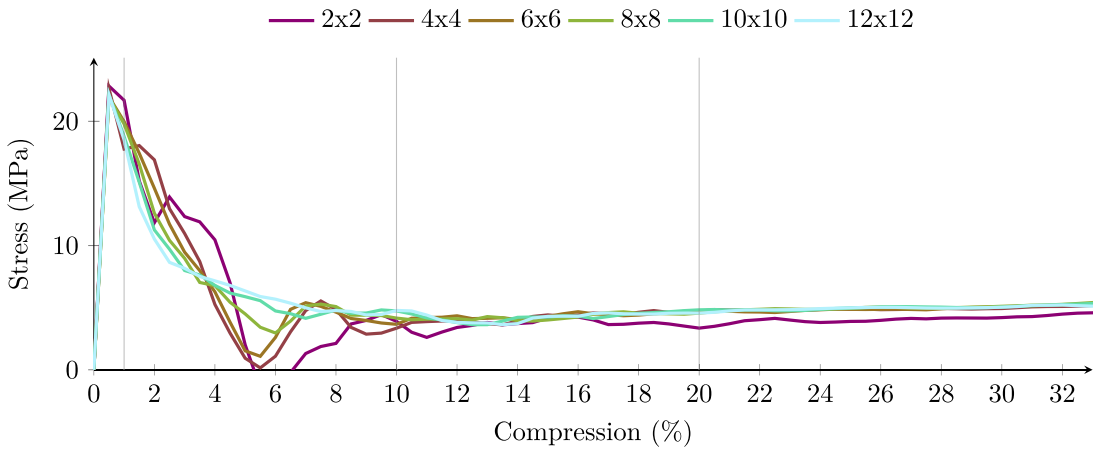

Fig. A.9. Stress–strain curves of patches with a different number of honeycombs unit cells under *slow* rate compression.

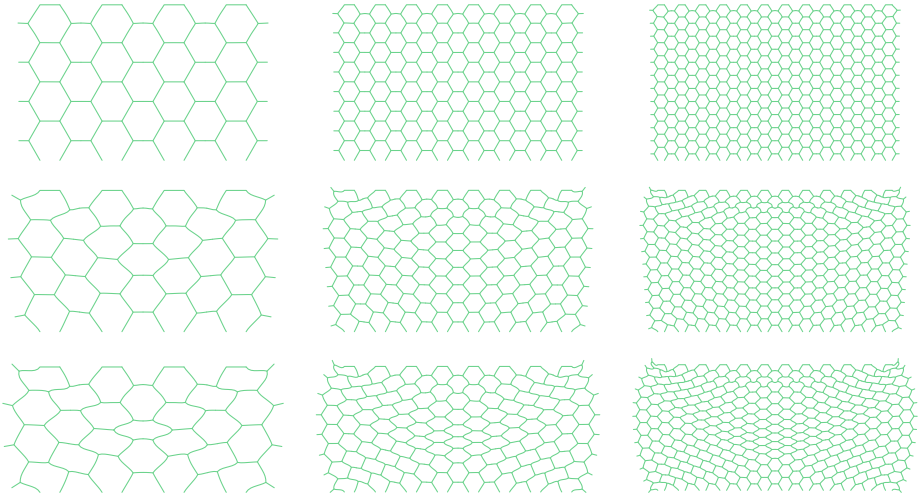

Fig. A.10. 4×4 (left), 8×8 (centre), and 12×12 (right) unit cell patches under *slow* rate deformation at 1 %, 10 % and 20 % compression.

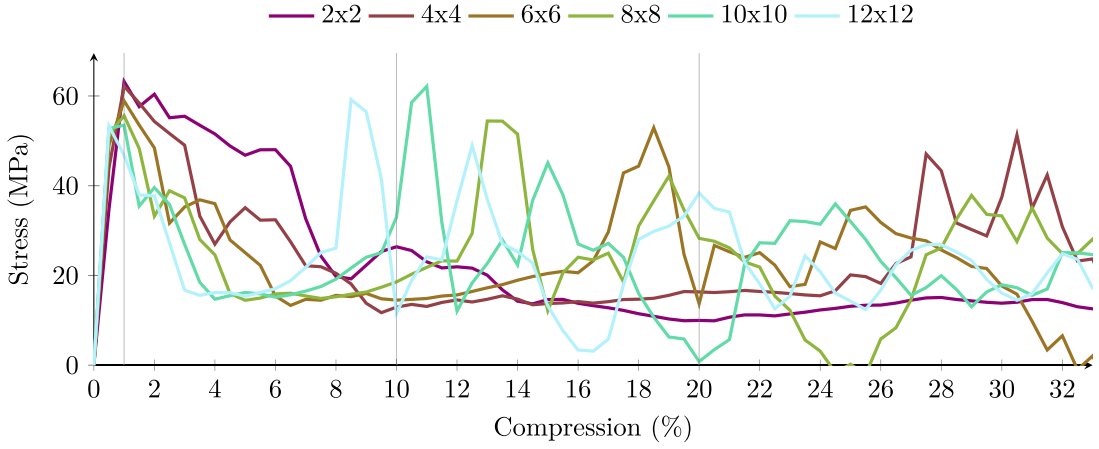

Fig. A.11. Stress–strain curves of patches with a different number of honeycombs unit cells under *medium* rate compression.

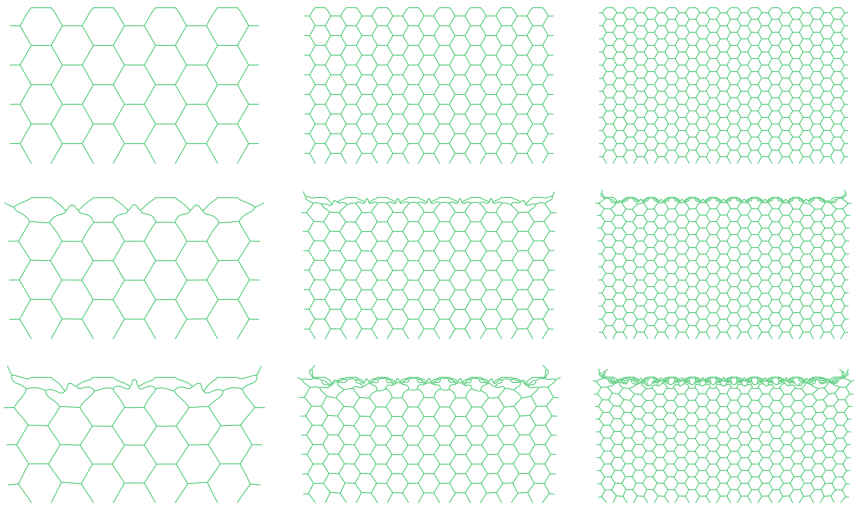

Fig. A.12. 4×4 (left), 8×8 (centre), and 12×12 (right) unit cell patches under *medium* rate deformation at 1 %, 10 % and 20 % compression.

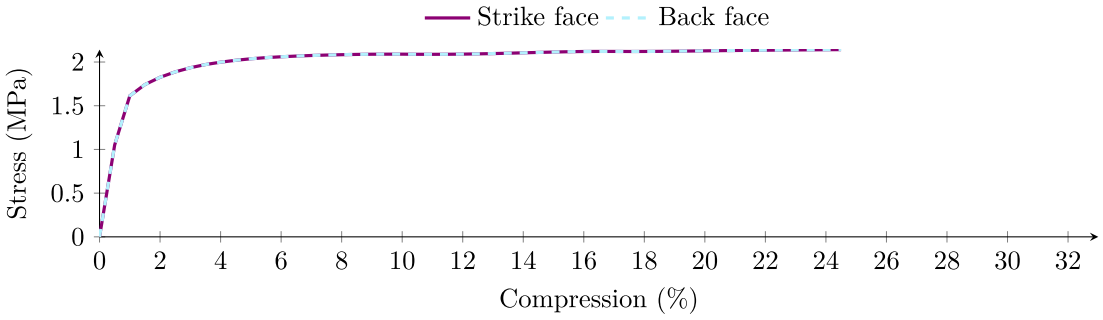

Fig. B.1. Comparison of the stress on the strike face and the back face under *static* compression for an 8×8 re-entrant patch.

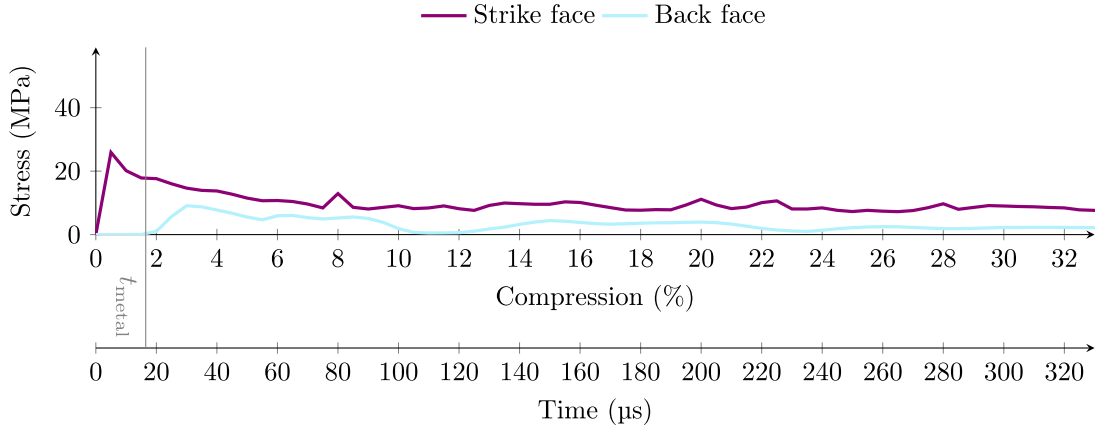

Fig. B.2. Comparison of the stress on the strike face and the back face under *medium* compression for an 8×8 re-entrant patch.

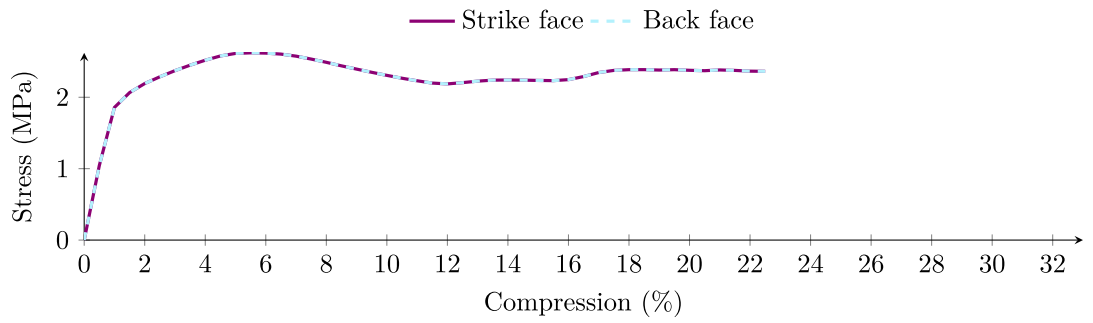

Fig. B.3. Comparison of the stress on the strike face and the back face under *static* compression for an 8×8 chiral patch.

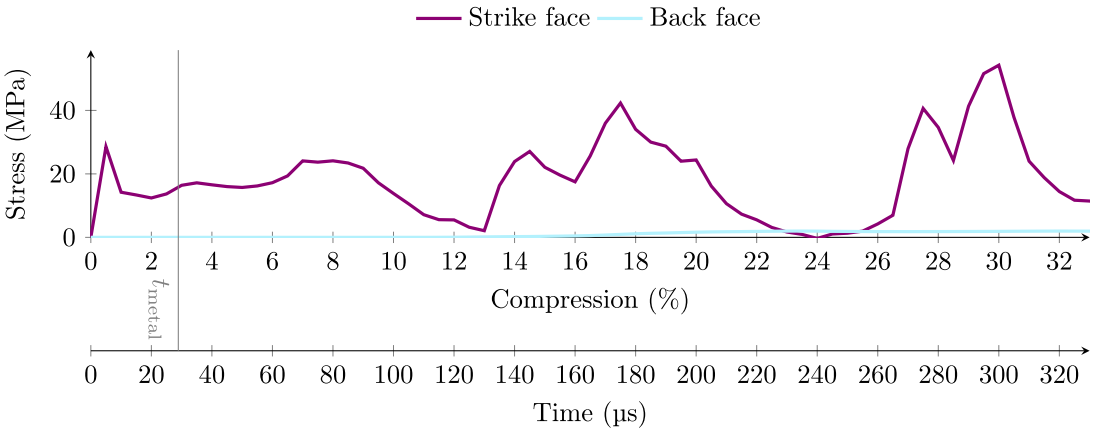

Fig. B.4. Comparison of the stress on the strike face and the back face under *medium* compression for an 8×8 chiral patch.

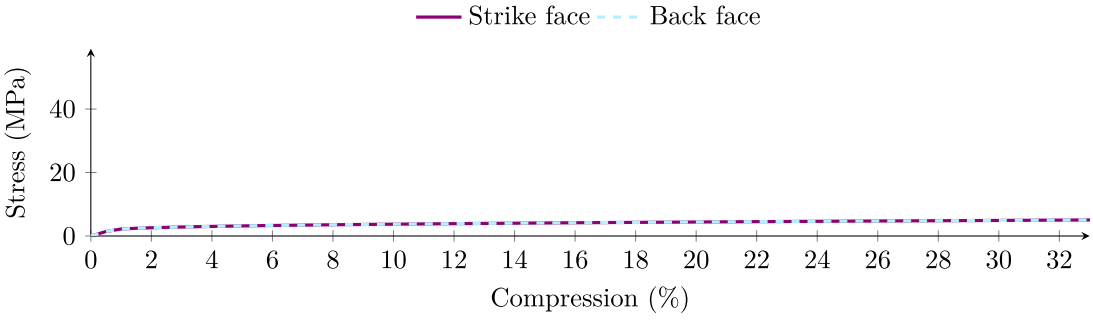

Fig. B.5. Comparison of the stress on the strike face and the back face under *static* compression for an 8×8 honeycomb patch.

B.3. Honeycomb patch

For the honeycomb patch, the time needed for a pressure stress wave to travel through the metal is computed from the height of the patch $h = 148\,\text{mm}$ and the angle between the beams and the vertical of $\alpha = 29.7°$: See Figs. B.5 and B.6.

$$t_{\text{metal}} = \frac{h/\cos(\alpha)}{c_{\text{metal}}} \approx 32.9\,\mu\text{s}. \tag{B.2}$$

Data availability

The code used in this study is available in the GitHub repository at https://github.com/hortulanusT/dynLattice. The raw data can be made available from the corresponding author upon reasonable request.

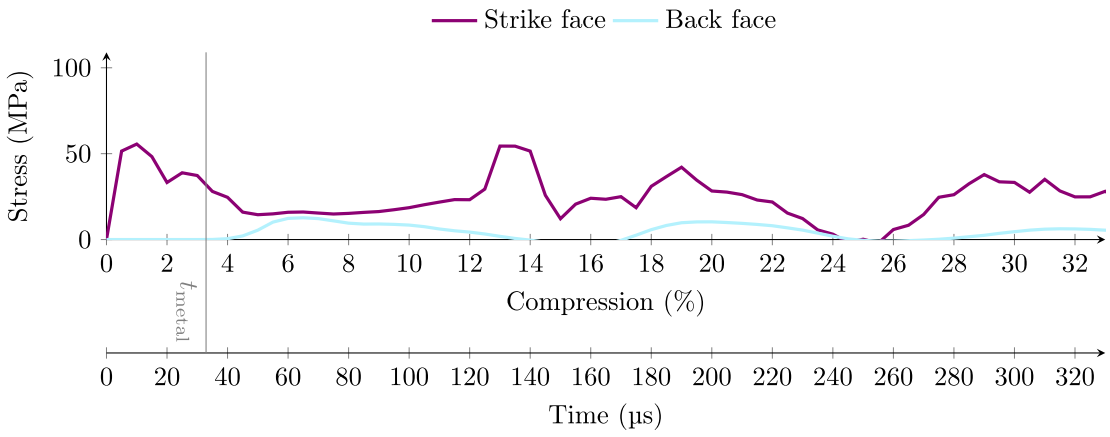

Fig. B.6. Comparison of the stress on the strike face and the back face under *medium* compression for an 8×8 honeycomb patch.

References

[1] P. Jiao, J. Mueller, J.R. Raney, X.R. Zheng, A.H. Alavi, Mechanical metamaterials and beyond, Nat. Commun. 14 (2023) 6004, http://dx.doi.org/10.1038/s41467-023-41679-8.

[2] S. Bonfanti, S. Hiemer, R. Zulkarnain, R. Guerra, M. Zaiser, S. Zapperi, Computational design of mechanical metamaterials, Nat. Comput. Sci. 4 (2024) 574–583, http://dx.doi.org/10.1038/s43588-024-00672-x.

[3] J.U. Surjadi, C.M. Portela, Enabling three-dimensional architected materials across length scales and timescales, Nat. Mater. 24 (2025) 493–505, http://dx.doi.org/10.1038/s41563-025-02119-8.

[4] M. Sanami, N. Ravirala, K. Alderson, A. Alderson, Auxetic materials for sports applications, Procedia Eng. 72 (2014) 453–458, http://dx.doi.org/10.1016/j.proeng.2014.06.079.

[5] C. Pardini, L. Anselmo, Assessing the risk of orbital debris impact, Space Debris 1 (1999) 59–80, http://dx.doi.org/10.1023/a:1010066300520.

[6] D. Saini, B. Shafei, Prediction of extent of damage to metal roof panels under hail impact, Eng. Struct. 187 (2019) 362–371, http://dx.doi.org/10.1016/j.engstruct.2019.02.036.

[7] J. Pan, H. Fang, M.C. Xu, Y.F. Wu, Study on the performance of energy absorption structure of bridge piers against vehicle collision, Thin-Walled Struct. 130 (2018) 85–100, http://dx.doi.org/10.1016/j.tws.2018.05.008.

[8] I.G. Crouch, Body armour - new materials, new systems, Def. Technol. 15 (2019) 241–253, http://dx.doi.org/10.1016/j.dt.2019.02.002.

[9] R.P. Bohara, S. Linforth, T. Nguyen, A. Ghazlan, T. Ngo, Anti-blast and -impact performances of auxetic structures: A review of structures, materials, methods, and fabrications, Eng. Struct. 276 (2023) http://dx.doi.org/10.1016/j.engstruct.2022.115377.

[10] D. Tahir, M. Zhang, H. Hu, Auxetic materials for personal protection: A review, Phys. Status Solidi (B) 259 (2022) http://dx.doi.org/10.1002/pssb.202200324.

[11] X. Ren, R. Das, P. Tran, T.D. Ngo, Y.M. Xie, Auxetic metamaterials and structures: a review, Smart Mater. Struct. 27 (2018) http://dx.doi.org/10.1088/1361-665X/aaa61c.

[12] K.K. Saxena, R. Das, E.P. Calius, Three decades of auxetics research – materials with negative Poisson's ratio: A review, Adv. Eng. Mater. 18 (2016) 1847–1870, http://dx.doi.org/10.1002/adem.201600053.

[13] I.I. Argatov, R. Guinovart-Díaz, F.J. Sabina, On local indentation and impact compliance of isotropic auxetic materials from the continuum mechanics viewpoint, Internat. J. Engrg. Sci. 54 (2012) 42–57, http://dx.doi.org/10.1016/j.ijengsci.2012.01.010.

[14] J.B. Choi, R.S. Lakes, Non-linear properties of metallic cellular materials with a negative Poisson's ratio, J. Mater. Sci. 27 (1992) 5375–5381, http://dx.doi.org/10.1007/bf02403846.

[15] J.B. Choi, R.S. Lakes, Fracture toughness of re-entrant foam materials with a negative Poisson's ratio: experiment and analysis, Int. J. Fract. 80 (1996) 73–83, http://dx.doi.org/10.1007/bf00036481.

[16] L. Jiang, H. Hu, Low-velocity impact response of multilayer orthogonal structural composite with auxetic effect, Compos. Struct. 169 (2017) 62–68, http://dx.doi.org/10.1016/j.compstruct.2016.10.018.

[17] T. Fu, X. Wang, X. Hu, T. Rabczuk, Impact dynamic response of stiffened porous functionally graded materials sandwich doubly-curved shells with arc-type auxetic core, Int. J. Impact Eng. 191 (2024) http://dx.doi.org/10.1016/j.ijimpeng.2024.105000.

[18] M.-F. Guo, H. Yang, L. Ma, 3D lightweight double arrow-head plate-lattice auxetic structures with enhanced stiffness and energy absorption performance, Compos. Struct. 290 (2022) http://dx.doi.org/10.1016/j.compstruct.2022.115484.

[19] T. Vitalis, A. Gross, S. Gerasimidis, Mechanical response and failure modes of three-dimensional auxetic re-entrant LPBF-manufactured steel truss lattice materials, J. Appl. Mech. 91 (2024) http://dx.doi.org/10.1115/1.4065669.

[20] C. Srivastava, V. Mahesh, P.J. Guruprasad, N. Petrinic, F. Scarpa, D. Harursampath, S.A. Ponnusami, Effect of damage evolution on the auxetic behavior of 2D and 3D re-entrant type geometries, Mech. Mater. (2024) http://dx.doi.org/10.1016/j.mechmat.2024.104980.

[21] Z. Liu, X. Luo, X. He, J. Liu, S. Yu, W. Huang, The dynamic response of composite auxetic re-entrant honeycomb structure subjected to underwater impulsive loading, Int. J. Impact Eng. (2024) http://dx.doi.org/10.1016/j.ijimpeng.2024.104999.

[22] W. Liu, N. Wang, T. Luo, Z. Lin, In-plane dynamic crushing of re-entrant auxetic cellular structure, Mater. Des. 100 (2016) 84–91, http://dx.doi.org/10.1016/j.matdes.2016.03.086.

[23] C. Qi, A. Remennikov, L.-Z. Pei, S. Yang, Z.-H. Yu, T.D. Ngo, Impact and close-in blast response of auxetic honeycomb-cored sandwich panels: Experimental tests and numerical simulations, Compos. Struct. 180 (2017) 161–178, http://dx.doi.org/10.1016/j.compstruct.2017.08.020.

[24] S. Farshbaf, N. Dialami, M. Cervera, Large deformation and collapse analysis of re-entrant auxetic and hexagonal honeycomb lattice structures subjected to tension and compression, 2025, http://dx.doi.org/10.1016/j.mechmat.2025.105457.

[25] T. Gärtner, S.J. van den Boom, J. Weerheijm, L.J. Sluys, Geometric effects on impact mitigation in architected auxetic metamaterials, Mech. Mater. 191 (2024) 104952, http://dx.doi.org/10.1016/j.mechmat.2024.104952.

[26] P.P. Meyer, C. Bonatti, T. Tancogne-Dejean, D. Mohr, Graph-based metamaterials: Deep learning of structure–property relations, Mater. Des. 223 (2022) http://dx.doi.org/10.1016/j.matdes.2022.111175.

[27] P.P. Meyer, T. Tancogne-Dejean, D. Mohr, Non-symmetric plate-lattices: Recurrent neural network-based design of optimal metamaterials, Acta Mater. 278 (2024) http://dx.doi.org/10.1016/j.actamat.2024.120246.

[28] R. Critchley, I. Corni, J.A. Wharton, F.C. Walsh, R.J.K. Wood, K.R. Stokes, A review of the manufacture, mechanical properties and potential applications of auxetic foams, Phys. Status Solidi (B) 250 (2013) 1963–1982, http://dx.doi.org/10.1002/pssb.201248550.

[29] T. Gärtner, R. Dekker, D. van Veen, S.J. van den Boom, L. Amaral, (in)efficacy of architected auxetic materials for impact mitigation, Int. J. Impact Eng. 206 (2025) http://dx.doi.org/10.1016/j.ijimpeng.2025.105402.

[30] C.R. Calladine, R.W. English, Strain-rate and inertia effects in the collapse of two types of energy-absorbing structure, Int. J. Mech. Sci. 26 (1984) 689–701, http://dx.doi.org/10.1016/0020-7403(84)90021-3.

[31] D. Ruan, G. Lu, B. Wang, T.X. Yu, In-plane dynamic crushing of honeycombs-a finite element study, Int. J. Impact Eng. 28 (2003) 161–182, http://dx.doi.org/10.1016/s0734-743x(02)00056-8.

[32] C. Coulais, C. Kettenis, M. van Hecke, A characteristic length scale causes anomalous size effects and boundary programmability in mechanical metamaterials, Nat. Phys. 14 (2017) 40–44, http://dx.doi.org/10.1038/nphys4269.

[33] J. Zhang, J. Liu, A. Souslov, M.T.P. Prado, J. Segurado, M. Haranczyk, J. Christensen, Buckle-barrel correspondence based on topological polarization conversion in mechanical metamaterials, Adv. Mater. 37 (2025) e2415962, http://dx.doi.org/10.1002/adma.202415962.

[34] L.J. Gibson, M.F. Ashby, G.S. Schajer, C.I. Robertson, The mechanics of two-dimensional cellular materials, Proc. R. Soc. Lond. A. Math. Phys. Sci. 382 (1997) 25–42, http://dx.doi.org/10.1098/rspa.1982.0087.

[35] C.W. Smith, J.N. Grima, K.E. Evans, A novel mechanism for generating auxetic behaviour in reticulated foams: missing rib foam model, Acta Mater. 48 (2000) 4349–4356, http://dx.doi.org/10.1016/s1359-6454(00)00269-x.

[36] Dynaflow Research Group, Jive, 2021, URL: https://dynaflow.com/software/jive/.
[37] E. Reissner, On finite deformations of space-curved beams, Z. Angew. Math. Phys. 32 (1981) 734–744, http://dx.doi.org/10.1007/Bf00946983.
[38] J.C. Simo, A finite strain beam formulation, the three-dimensional dynamic problem. part I, Comput. Methods Appl. Mech. Engrg. 49 (1985) 55–70, http://dx.doi.org/10.1016/0045-7825(85)90050-7.
[39] Smriti A. Kumar, A. Großmann, P. Steinmann, A thermoelastoplastic theory for special cosserat rods, Math. Mech. Solids 24 (2018) 686–700, http://dx.doi.org/10.1177/1081286517754132.
[40] T. Gärtner, S.J. van den Boom, J. Weerheijm, L.J. Sluys, A strategy for scaling the hardening behavior in finite element modelling of geometrically exact beams, Comput. Mech. 75 (2025) 1471–1482, http://dx.doi.org/10.1007/s00466-024-02572-3.
[41] L. Herrnböck, A. Kumar, P. Steinmann, Geometrically exact elastoplastic rods: determination of yield surface in terms of stress resultants, Comput. Mech. 67 (2021) 723–742, http://dx.doi.org/10.1007/s00466-020-01957-4.
[42] L. Herrnböck, A. Kumar, P. Steinmann, Two-scale off-and online approaches to geometrically exact elastoplastic rods, Comput. Mech. 71 (2022) 1–24, http://dx.doi.org/10.1007/s00466-022-02204-8.
[43] J.C. Simo, L. Vu-Quoc, A three-dimensional finite-strain rod model. part II: Computational aspects, Comput. Methods Appl. Mech. Engrg. 58 (1986) 79–116, http://dx.doi.org/10.1016/0045-7825(86)90079-4.
[44] M.A. Crisfield, G. Jelenić, Objectivity of strain measures in the geometrically exact three-dimensional beam theory and its finite-element implementation, Proc. R. Soc. A-Math. Phys. Eng. Sci. 455 (1999) 1125–1147, http://dx.doi.org/10.1098/rspa.1999.0352.
[45] P. Wriggers, J.C. Simo, A note on tangent stiffness for fully nonlinear contact problems, Commun. Appl. Numer. Methods 1 (1985) 199–203, http://dx.doi.org/10.1002/cnm.1630010503.
[46] W.E. Milne, Numerical integration of ordinary differential equations, Am. Math. Mon. 33 (1926) http://dx.doi.org/10.1080/00029890.1926.11986619.
[47] H.Z. Munthe-Kaas, Lie Group Integrators, Springer Berlin Heidelberg, 2015, pp. 787–790, http://dx.doi.org/10.1007/978-3-540-70529-1_122.
[48] B.C. White, A. Garland, R. Alberdi, B.L. Boyce, Interpenetrating lattices with enhanced mechanical functionality, Addit. Manuf. 38 (2021) http://dx.doi.org/10.1016/j.addma.2020.101741.
[49] K.M. Fitzgerald, R.G. Smith, K.L. Johnson, J.H.J. Niederhaus, J.A. Dye, B.L. Boyce, K.T. Strong, B.C. White, Structural metamaterials with innate capacitive and resistive sensing, J. Mater. Sci. 59 (2024) 15469–15490, http://dx.doi.org/10.1007/s10853-024-10097-6.
[50] G. Qi, J.-j. Tian, C.-x. Liu, Y.-l. Chen, S. Jiang, Z.-j. He, M. Han, K.-U. Schröder, L. Ma, Compressive properties of aperiodic but ordered cellular materials inspired by penrose tilings, Thin-Walled Struct. 204 (2024) http://dx.doi.org/10.1016/j.tws.2024.112287.
[51] M.I.N. Rosa, K. Karapiperis, K. Radi, E. Pescialli, D.M. Kochmann, Enhanced deformability through distributed buckling in stiff quasicrystalline architected materials, Adv. Mater. (2025) e2505125, http://dx.doi.org/10.1002/adma.202505125.
[52] DelftBlue supercomputer (phase 2), 2024, https://www.tudelft.nl/dhpc/ark:/44463/DelftBluePhase2.
[53] F. Crameri, Scientific colour maps, 2023, http://dx.doi.org/10.5281/zenodo.8409685.